



Three-dimensional chromatin landscapes in T cell acute lymphoblastic leukemia

Andreas Kloetgen^{1,2,13}, Palaniraja Thandapani^{1,2,13}, Panagiotis Ntziachristos^{1,2,3,4,13}, Yohana Ghebrechristos^{1,2}, Sofia Nomikou^{1,2}, Charalampos Lazaris^{1,2}, Xufeng Chen^{1,2}, Hai Hu^{1,2}, Sofia Bakogianni^{1,5}, Jingjing Wang^{1,2}, Yi Fu^{1,2}, Francesco Boccalatte^{1,2}, Hua Zhong⁷, Elisabeth Paietta⁸, Thomas Trimarchi^{1,2,9}, Yixing Zhu³, Pieter Van Vlierberghe^{1,2,10}, Giorgio G. Inghirami^{1,2}, Timothee Lionnet⁶, Iannis Aifantis^{1,2,14} and Aristotelis Tsirigos^{1,2,12,14}

Differences in three-dimensional (3D) chromatin architecture can influence the integrity of topologically associating domains (TADs) and rewire specific enhancer-promoter interactions, impacting gene expression and leading to human disease. Here we investigate the 3D chromatin architecture in T cell acute lymphoblastic leukemia (T-ALL) by using primary human leukemia specimens and examine the dynamic responses of this architecture to pharmacological agents. Systematic integration of matched *in situ* Hi-C, RNA-seq and CTCF ChIP-seq datasets revealed widespread differences in intra-TAD chromatin interactions and TAD boundary insulation in T-ALL. Our studies identify and focus on a TAD ‘fusion’ event associated with absence of CTCF-mediated insulation, enabling direct interactions between the MYC promoter and a distal super-enhancer. Moreover, our data also demonstrate that small-molecule inhibitors targeting either oncogenic signal transduction or epigenetic regulation can alter specific 3D interactions found in leukemia. Overall, our study highlights the impact, complexity and dynamic nature of 3D chromatin architecture in human acute leukemia.

The human genome is replete with regulatory elements such as promoters, enhancers and insulators. Recent findings have highlighted the impact of spatial genome organization in governing the physical proximity of these elements for the precise control of gene expression^{1–3}. Genome organization is a multistep process that involves compacting chromatin into nucleosomes, chromatin fibers, compartments and chromosome territories^{3,4}. Multiple lines of evidence have suggested that, at the sub-megabase level, the genome is organized in distinct regions of highly self-interacting chromatin called TADs^{5–7}. An important function of TADs is to restrict the interactions of regulatory elements to genes within the same TAD, while insulating them from interactions with neighboring domains^{3,4}. Further evidence from our laboratory suggests that super-enhancers, which often regulate key genes determining cellular identity or driving tumorigenesis^{8,9}, are frequently insulated by and co-duplicated with strong TAD boundaries in cancer¹⁰. TAD boundaries are enriched in binding of structural proteins (CTCF and cohesin)¹¹. Cohesin-mediated, convergently oriented CTCF-CTCF structural loops are essential for the organization of the genome into TADs^{12–14}. Abrogation of CTCF binding or inversion of its orientation in boundary regions can change TAD structure and reconfigure enhancer-promoter interactions¹⁵, leading to aberrant gene activation and developmental defects^{1,16}.

In light of these reports, understanding how chromatin organization contributes to cancer pathogenesis remains largely unexplored, barring a few examples^{2,17,18}. Here, by using T-ALL as a model^{19,20}, we investigated potential reorganization of global chromatin architecture in primary T-ALL samples, T-ALL cell lines and healthy peripheral T cells. Our analysis identified recurrent structural differences at TAD boundaries and significant alterations in intra-TAD chromatin interactions that mirrored differences in gene expression. Both types of alterations affected effectors of oncogenic NOTCH1 signaling. As a principal example, we identified a recurrent TAD boundary change in T-ALL within the locus of a key driver of T cell leukemogenesis, MYC, which facilitates long-range interactions of the MYC promoter with a previously characterized NOTCH-bound super-enhancer. Furthermore, highlighting a direct role for NOTCH1 in organizing chromatin architecture, inhibition of NOTCH1 signaling using gamma-secretase inhibitors (γ SI) reduced chromatin looping in a number of enhancer-promoter pairs that are sensitive to γ SI treatment (called ‘dynamic NOTCH1’ sites²¹). Loss of chromatin interactions between enhancer-promoter loops was associated with a reduction in acetylation at histone H3 lysine 27 (H3K27ac) at the respective enhancer. However, a subset of enhancer-promoter loops, including the MYC-super-enhancer loop, retained their interactions with target promoters after γ SI

¹Department of Pathology, New York University School of Medicine, New York, NY, USA. ²Laura and Isaac Perlmutter Cancer Center, New York University School of Medicine, New York, NY, USA. ³Department of Biochemistry and Molecular Genetics, Feinberg School of Medicine, Northwestern University, Chicago, IL, USA. ⁴Robert H. Lurie Comprehensive Cancer Center, Northwestern University, Chicago, IL, USA. ⁵Department of Microbiology, New York University School of Medicine, Alexandria Center for Life Sciences, New York, NY, USA. ⁶Department of Cell Biology, Institute for Systems Genetics, New York University, New York, NY, USA. ⁷Division of Biostatistics, Department of Population Health, New York University School of Medicine, New York, NY, USA. ⁸Montefiore Medical Center, New York, NY, USA. ⁹BridgeBio Pharma, Palo Alto, CA, USA. ¹⁰Department of Biomolecular Medicine, Ghent University, Ghent, Belgium. ¹¹Department of Pathology and Laboratory Medicine, Weill Cornell Medicine, New York, NY, USA. ¹²Applied Bioinformatics Laboratories, Office of Science and Research, New York University School of Medicine, New York, NY, USA. ¹³These authors contributed equally: Andreas Kloetgen, Palaniraja Thandapani, Panagiotis Ntziachristos. ¹⁴These authors jointly supervised this work: Iannis Aifantis, Aristotelis Tsirigos. [✉]e-mail: ioannis.aifantis@nyulangone.org; aristotelis.tsirigos@nyulangone.org

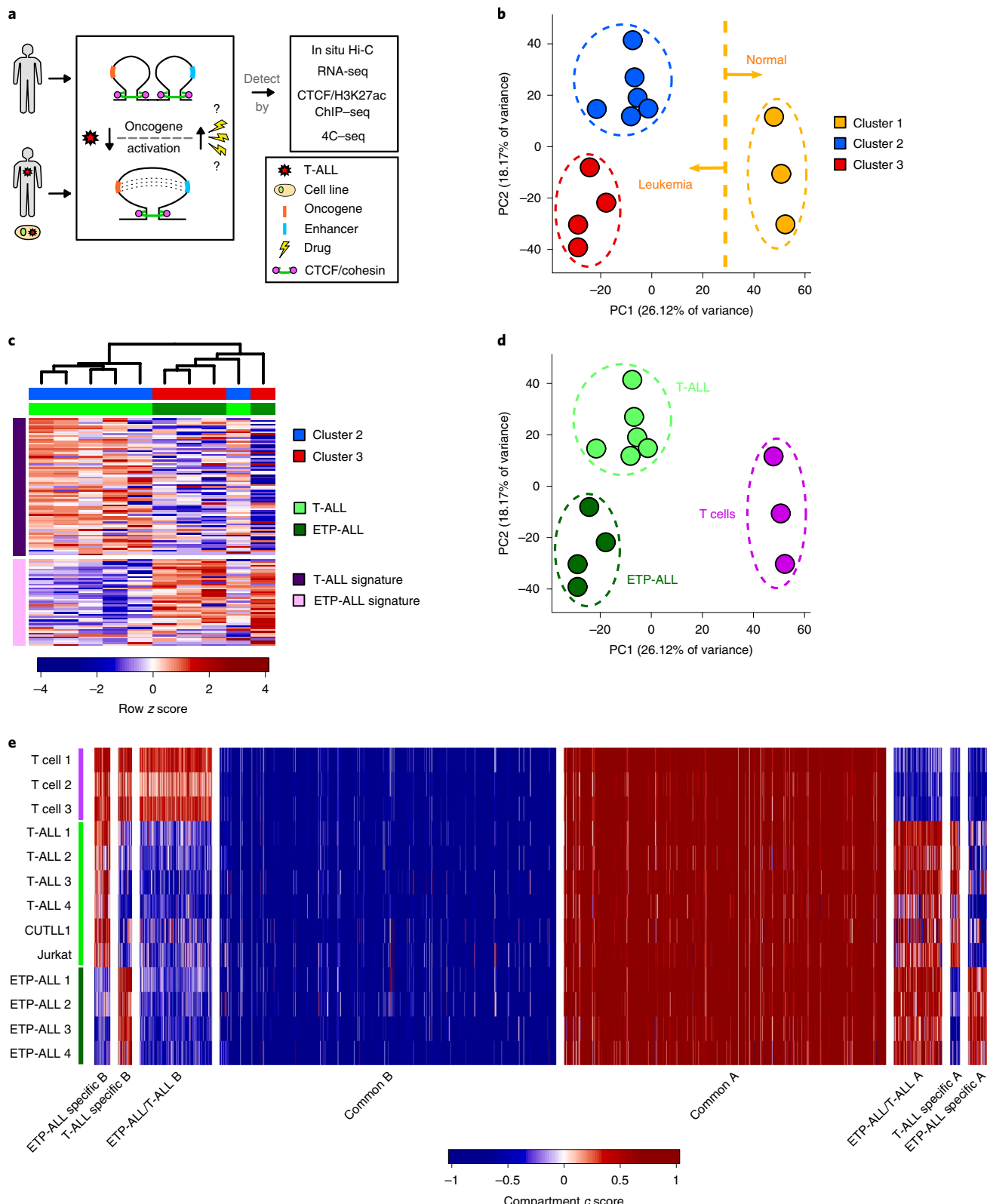


Fig. 1 | In situ Hi-C analysis identifies genome-wide 3D chromatin differences between normal T cells and T-ALL subtypes. **a**, Schematic showing the overall study design. **b**, PCA of the hic-ratio insulation scores for each Hi-C dataset ($n=13$) identifies three distinct clusters. Clustering was performed by using the R package Mclust, with the EII and VII models showing optimal separation when using three clusters. **c**, Heat map representation of RNA-seq results for clusters 2 and 3 separated by T-ALL and ETP-ALL gene signature (rows). Gene signatures were derived from the RNA-seq results in refs. 24,26,30. The heat map shows the row z score of FPKM normalized read counts determined by using the edgeR function rpkm. **d**, PCA of hic-ratio insulation scores as in **b** ($n=13$); samples are colored by cell type assignment determined with the help of RNA-seq data. **e**, Compartment analysis using c score on all Hi-C datasets ($n=13$). Different categories of disease-specific and common compartment switches were identified by unpaired two-sided t tests on c scores from comparisons between T-ALL, ETP-ALL and T cells ($P < 0.1$).

treatment, despite being bound by NOTCH1. In exploring putative cofactors maintaining long-range interactions, we identified CDK7 binding to be enriched in γSI-insensitive chromatin contacts. Pharmacological inhibition of CDK7 using the covalent inhibitor THZ1 significantly reduced *MYC* promoter contacts with the super-enhancer, underlining the complexity of the factors regulating 3D architecture. Taken together, our findings provide deeper insight into how 3D chromatin architecture can affect the regulatory landscape of oncogenes in human leukemia and suggest that some of the changes can be inhibited by targeted drug treatments.

Results

Widespread changes in 3D chromatin landscape in human T-ALL. T-ALL accounts for approximately 25% of ALL cases²² and is characterized by activating mutations in *NOTCH1* in approximately 50% of patients^{23,24}. On the basis of gene expression signatures and immunophenotyping, T-ALL is classified into two subtypes, including ‘canonical’ T-ALL, characterized by frequent *NOTCH1* mutations with an immature T cell phenotype, and the early T-lineage progenitor (ETP) leukemia subtype, frequently expressing stem cell and myeloid cell-surface markers^{25,26}. Although the genetic drivers of T-ALL are well characterized, it has not been investigated whether malignant transformation of immature T cells is associated with widespread changes in chromatin architecture. Herein, to broadly assess the global chromatin architecture in T-ALL, we performed *in situ* Hi-C in eight primary peripheral blood T-ALL samples, T-ALL cell lines (CUTLL1 (ref. ²⁷) and Jurkat²⁸ cells) and mature peripheral blood T cells from three healthy donors. We integrated these datasets with CTCF binding, RNA expression and enhancer activity (Fig. 1a). The Hi-C data, processed by our HiC-bench platform²⁹, showed alignment rates with a high percentage of usable long-range read pairs (Extended Data Fig. 1a and Supplementary Table 1). Principal-component analysis (PCA) of genome-wide ‘hic-ratio’ insulation scores (from the HiC-bench platform), representing the insulation capacity of each genome-wide bin, indicated three distinct clusters of samples clearly separated by the first two components (Fig. 1b). Cluster 1 samples were identified as mature peripheral T cells and were separated from T-ALL samples (clusters 2 and 3) by the first principal component. To discern the identity of clusters 2 and 3, we interrogated the expression patterns of these samples by using gene signatures for canonical T-ALL and ETP-ALL^{24,26,30}. Among the T-ALL samples, the four T-ALL samples grouped in cluster 3 were identified to share a characteristic gene

signature of the ETP-ALL subtype (Fig. 1c). The expression of cluster 2 samples overlapped with that of canonical T-ALL, with a single exception (Supplementary Note). Thus, assignment of canonical T-ALL and ETP-ALL using gene expression information explains the variation in Hi-C insulation scores between clusters 2 and 3 (Fig. 1d). Additionally, we calculated matrix-wide stratum-adjusted correlation coefficients by using HiCRep³¹ between the Hi-C contact matrices for all pairwise comparisons. We observed higher correlation among the T cells and among the two T-ALL subtypes (Extended Data Fig. 1b), further supporting genome-wide variations in 3D architecture between the T cells and T-ALL samples, but also between the two distinct T-ALL subtypes. To better characterize differences in 3D architecture that underlie this separation, we first examined compartmentalization of the genome between the three clusters of Hi-C samples (Supplementary Note). Compartment shifts both common and unique to the T-ALL subtypes were identified relative to T cells (Extended Data Fig. 1c). We also identified strong correlations of compartment shifts with expression changes (Fig. 1e, Extended Data Fig. 1d,e and Supplementary Table 3). Collectively, these data show that differences in 3D architecture occur between T cells and T-ALL and also between subtypes of human T-ALL.

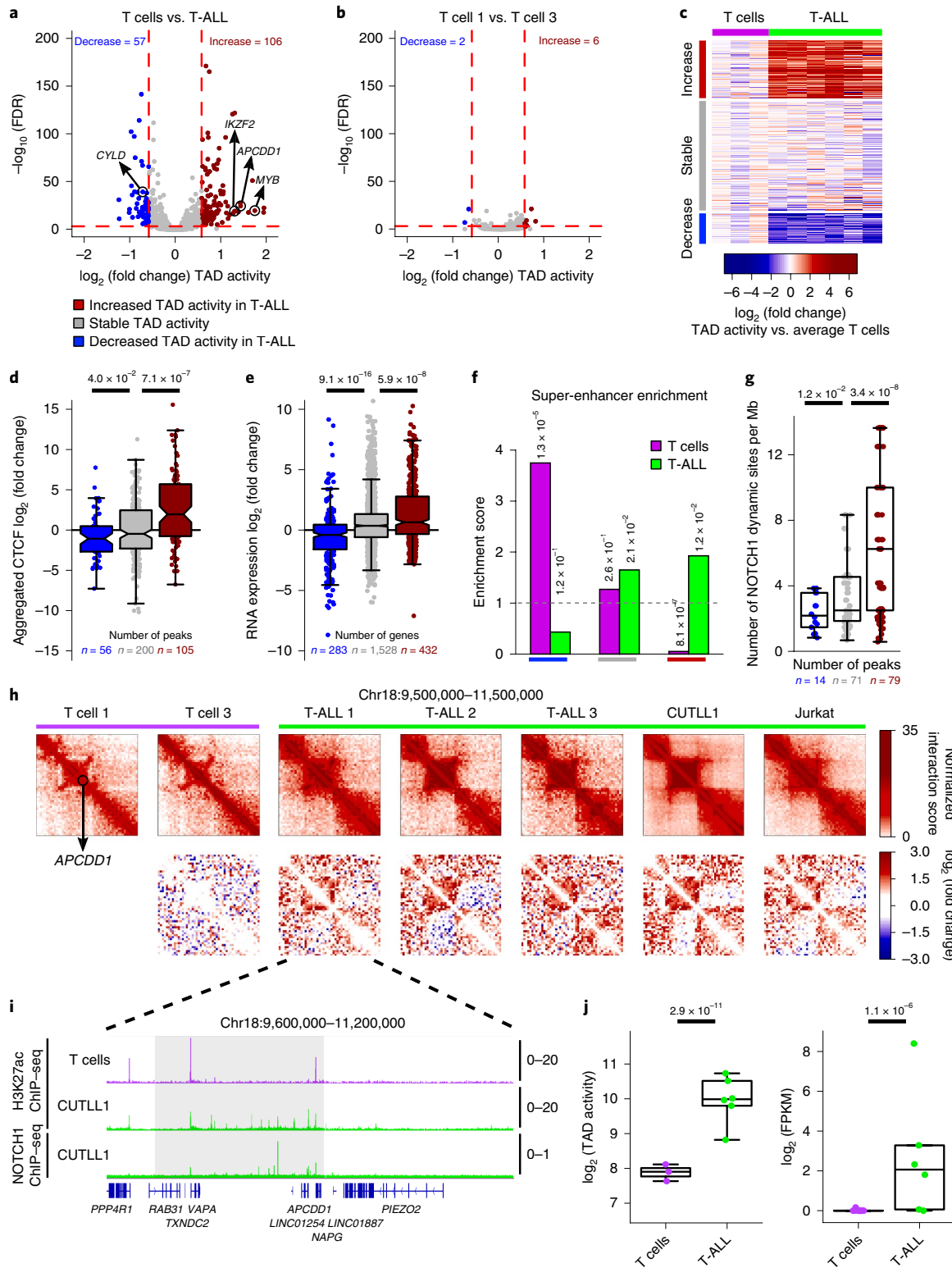
Intra-TAD activity differences affect downstream effectors of T-ALL pathogenesis. We then focused on all common TADs between T cells and T-ALL found within the transcriptionally active A compartment in either T cells or T-ALL. We defined ‘intra-TAD activity’ as the average of the normalized interaction scores for all interactions within the particular TAD. Differences in intra-TAD activity were determined by comparing the fold change in average intra-TAD activity between all T cell samples and the four primary canonical T-ALL samples (Supplementary Methods). Comparison of intra-TAD activity between canonical T-ALL samples and controls identified several statistically significant increases and decreases (Fig. 2a and Supplementary Table 4; false-discovery rate (FDR) < 0.1 and \log_2 (fold change) > 0.58 or < -0.58), whereas comparison between two independent T cell samples identified only a few changes when applying the same thresholds (Fig. 2b). Furthermore, the TAD activity changes were highly similar across primary canonical T-ALL samples and T-ALL cell lines (Fig. 2c), with some expected heterogeneity. Only ~16–18% of the identified intra-TAD activity changes had concomitant compartment shifts, with the majority falling in the A compartment in both T cells and T-ALL samples (Supplementary Fig. 1a). Additionally, TAD activity

Fig. 2 | Intra-TAD activity changes affect downstream effectors of T-ALL pathogenesis. **a**, Volcano plot showing differential intra-TAD activity for comparisons of T cells versus canonical T-ALL (all TADs, $n=1,027$). Statistical evaluation was performed by paired two-sided t test pairing each interaction bin per TAD between the averages of T cells and canonical T-ALL, followed by multiple-testing correction. **b**, Volcano plot of the same analysis as in **a** between two independent T cell Hi-C samples (all TADs, $n=1,027$). **c**, Heat map showing average per-sample intra-TAD activity in T-ALL and T cells normalized by the average intra-TAD activity across all three T cell samples. Rows show differentially active and stable TADs as highlighted in **a**. **d**, Integration of CTCF binding with the TAD boundary categories from **a**. All CTCF binding peaks from surrounding TAD boundaries were aggregated, and the \log_2 (fold change) in CTCF signal between T-ALL and T cells is shown. Significant differences were calculated by unpaired one-sided t test comparing TADs with decreased or increased intra-TAD activity to stable TADs. **e**, Integration of RNA expression (FPKM > 1) within TADs with decreased or increased intra-TAD activity. For each gene, the \log_2 (fold change) in expression between T-ALL and T cells from RNA-seq data is shown. Significant differences were calculated by unpaired one-sided t test comparing genes from TADs with decreased or increased intra-TAD activity to genes from stable TADs. **f**, Super-enhancer integration with differentially active TADs. Enrichment score was calculated as the observed overlap between super-enhancers and differentially active versus stable TADs over expected background. Statistical enrichment was calculated by two-sided Fisher’s exact test. **g**, Number of dynamic NOTCH1-binding sites per 1 Mb within TADs of decreased, stable or increased intra-TAD activity as defined in **a**. Significant differences for TADs with increased or decreased activity versus stable TADs were identified by unpaired two-sided t test. **h**, The top row shows Hi-C interaction heat maps. The bottom row shows heat maps of per-bin \log_2 (fold change) in interactions when compared to the T cell 1 sample. **i**, H3K27ac and NOTCH1 ChIP-seq tracks for the *APCDD1* locus, with data shown as fold enrichment over input. The gray area indicates TAD containing *APCDD1*. Number of replicates: T cells H3K27ac, $n=2$; CUTLL1 H3K27ac, $n=2$; CUTLL1 NOTCH1, $n=1$. **j**, Quantification of intra-TAD activity (left; area as highlighted in **i**) and expression of *APCDD1* (right). Statistical evaluation for intra-TAD activity was performed by paired two-sided t test comparing the average per interaction bin for the *APCDD1* TAD between T cells ($n=3$) and T-ALL ($n=6$), followed by multiple-testing correction. *APCDD1* expression was determined by RNA-seq and is shown as the \log_2 (FPKM) for T cell ($n=13$) and T-ALL ($n=6$) samples; normalization and statistical evaluation were performed with edgeR followed by multiple-testing correction. Box-plot information can be found in the Source Data.

changes were minimally impacted by genomic alterations such as translocations and copy number variants (Supplementary Note).

To further characterize differential intra-TAD activity between T-ALL and T cells, we integrated CTCF binding (chromatin immunoprecipitation and sequencing, ChIP-seq) with our Hi-C datasets. Interestingly, changes in intra-TAD activity strongly correlated with CTCF binding changes at the boundaries of differentially active TADs. Stronger insulation by CTCF was associated with stronger

intra-TAD activity (Fig. 2d). Next, to investigate whether CTCF-binding-associated differences in intra-TAD interactions were also associated with changes in gene expression, we performed differential expression analysis of all expressed genes (FPKM > 1, canonical T-ALL versus T cells) within differentially active TADs. Increased chromatin interactions in T-ALL significantly associated with positive fold changes in gene expression, whereas decreased intra-TAD activity in T-ALL associated with negative fold changes



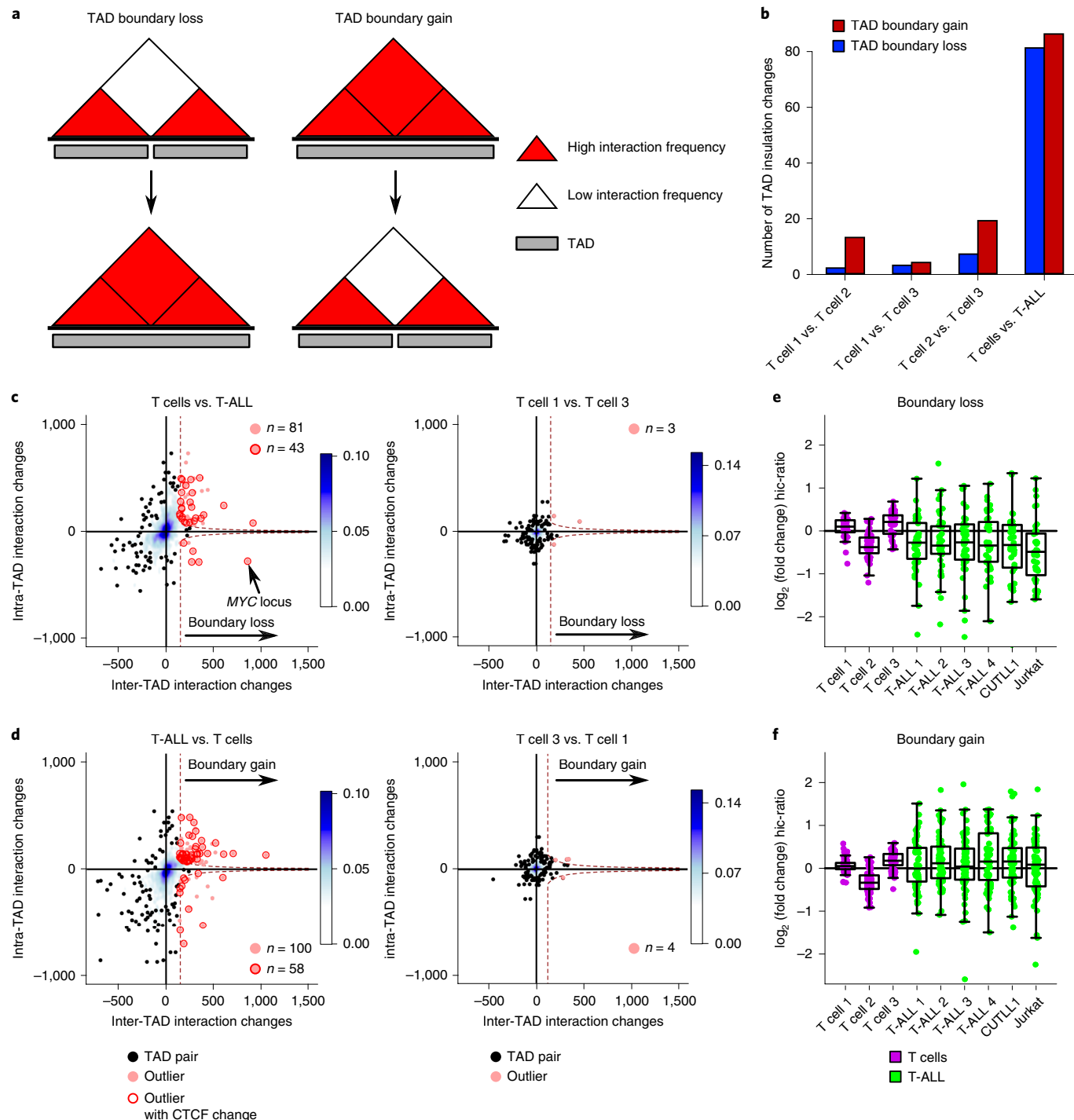


Fig. 3 | TAD boundary insulation analysis reveals changes in insulation of neighboring TADs. **a**, Schematic depicting TAD boundary insulation alteration events. **b**, Total number of TAD boundary gains and losses identified between T-ALL and T Cells. **c,d**, Density plot showing TAD insulation alteration events (red dots) among all pairs of adjacent TADs (black dots; $n=2,160$ for boundary loss and $n=2,772$ for boundary gain; blue shading indicates density of dots). Plots in **c** depict comparisons for TAD boundary loss of adjacent T cell TADs within T-ALL samples (left) and between T cell samples 1 and 3 (right). Plots in **d** depict comparisons for TAD boundary gain of adjacent T-ALL TADs when compared to T cell samples (left) and between T cell samples 1 and 3 (right). Circled adjacent TADs correspond to outliers of increased or decreased insulation accompanied by at least one increased or decreased CTCF binding peak, respectively. Significant changes in CTCF binding were calculated by using the R package DiffBind with the edgeR method and were filtered for FDR < 0.1 and \log_2 (fold change) > 1 or < -1. **e,f**, All TAD boundary alterations, including boundary loss (**e**) and boundary gain (**f**), from comparisons in **c** and **d** between T-ALL and T cells were used to estimate heterogeneity. Hic-ratio insulation scores for each boundary and sample were compared to the average hic-ratio insulation score for all T cell samples. Boundary losses ($n=81$) came with a decrease in insulation score on average, whereas boundary gains ($n=86$) came with an increase in insulation score across all T-ALL samples on average when compared to the average hic-ratio insulation score for all T cell samples. Box-plot information can be found in the Source Data.

in gene expression relative to expression changes within stable TADs (Fig. 2e). We then overlapped intra-TAD activity results with cell-type-specific super-enhancer occurrence in T-ALL and T cells (Supplementary Note). We found significant enrichment of T-ALL-specific super-enhancers within TADs of increased activity in T-ALL and vice versa (Fig. 2f). Additionally, TADs with higher activity in T-ALL were significantly enriched in dynamic NOTCH1-binding sites²¹, whereas TADs with lower activity in T-ALL were significantly depleted of dynamic NOTCH1-binding sites in comparison to stably active TADs (Fig. 2g). Taken together, these results demonstrate widespread changes in intra-TAD activity in T-ALL when compared to peripheral T cells that are associated with CTCF binding, mRNA expression and super-enhancer activity. Furthermore, we identified single-nucleotide variants to have minimal impact on the observed differential CTCF binding (Supplementary Fig. 1f).

Our comparison of changes in TAD activity and super-enhancer firing suggests that 3D chromosomal changes potentially occur in loci important for T-ALL pathogenesis, including loci with NOTCH1 target genes highly expressed in samples from individuals with T-ALL. One such gene is *APCDD1* (adenomatous polyposis coli downregulated 1), encoding a membrane-bound glycoprotein overexpressed in samples from individuals with T-ALL. *APCDD1* is a NOTCH1 target gene significantly downregulated following inhibition of NOTCH1 signaling by γSI (dynamic NOTCH1 target)²¹. Our Hi-C data showed *APCDD1* to be present in a highly active TAD in T-ALL (Fig. 2h,j), which was common among all the T-ALL samples and displayed concomitant enhancer elements in T-ALL (Fig. 2i). The gain of TAD activity also correlated with increased expression of *APCDD1* in T-ALL samples relative to T cells (Fig. 2j). Another example of a T-ALL-specific increase in intra-TAD activity, enhancer activity and gene expression was the Ikaros family gene *IKZF2* (Helios), previously found to be involved in the regulation of T cell differentiation³². We identified a T-ALL-specific super-enhancer within the same TAD, as well as significantly increased gene expression in T-ALL as compared to T cells (Extended Data Fig. 2a–c). In contrast, among the TADs that lost activity in T-ALL, we identified *CYLD*, encoding a deubiquitinating enzyme that represses NF-κB signaling and is known as a T-ALL tumor suppressor^{33,34}. We found significant reduction of interactions in the TAD that harbors *CYLD* in all profiled T-ALL samples (Extended Data Fig. 2d,e). The reduced TAD activity also correlated with reduced expression in T-ALL samples (Extended Data Fig. 2f). Extending our analysis, we also identified subtype-specific differences in intra-TAD activity between the canonical T-ALL and ETP-ALL samples (Supplementary Note).

Identification of recurrent TAD insulation changes in T-ALL.

Following our intra-TAD activity analysis, we investigated TAD

boundary changes between normal T cells and T-ALL. A TAD boundary ‘loss’ was defined as an increase in inter-TAD interactions between two adjacent TADs leading to a TAD ‘fusion’. Conversely, a TAD boundary ‘gain’ was defined as a decrease in inter-TAD interactions between two adjacent TADs leading to a TAD ‘separation’ (Fig. 3a and Supplementary Methods). Global analysis of alterations in TAD insulation revealed TAD boundary changes in both directions (Fig. 3a), whereas pairwise comparison of T cells from independent donors identified only a few TAD boundary alterations. However, considering all such insulation changes between the T cell samples as false positives, we estimated an approximate FDR of 9.58% for TAD boundary changes in T-ALL as compared to T cells (Fig. 3b). Furthermore, about 53–58% of TAD boundary differences were accompanied by simultaneous changes in CTCF binding within the respective boundaries (Fig. 3c,d). For an independent validation of these findings, we calculated the hic-ratio insulation score for all TAD boundary alterations found in comparison of T-ALL samples and T cells. The hic-ratio insulation score was on average increased and decreased for TAD boundary gains and losses, respectively, across all T-ALL samples (Fig. 3e,f). Very few of the observed TAD insulation changes overlapped with genomic alterations such as deletions or insertions (Supplementary Note).

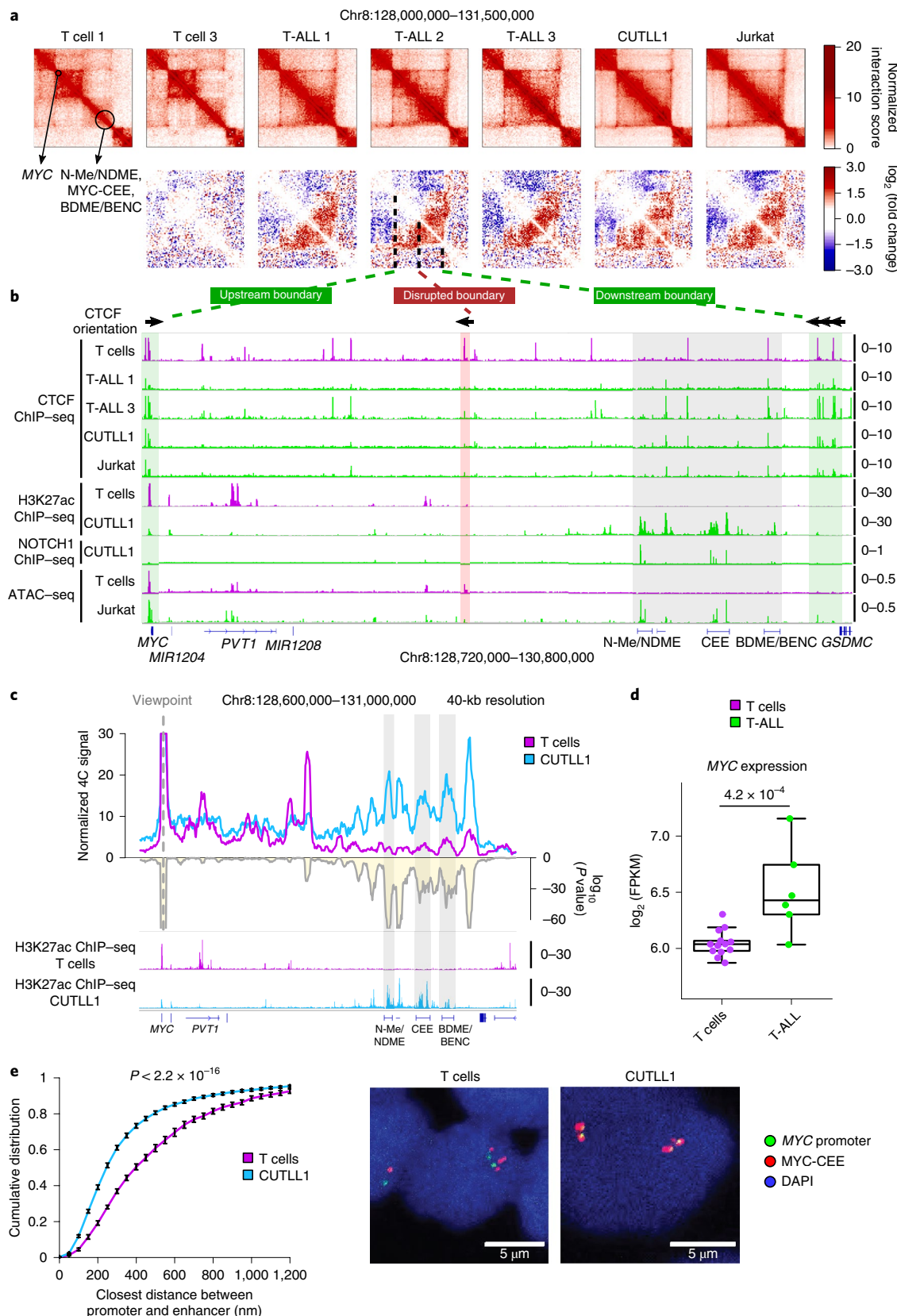
CTCF-mediated TAD insulation defines accessibility of MYC promoter-super-enhancer looping. *MYC* expression is significantly upregulated in T-ALL, and *MYC* is one of the main oncogenes activated downstream of NOTCH1 signaling^{35,36}. Intriguingly, we identified a recurrent TAD fusion in the *MYC* locus in all T-ALL samples as compared to T cells (Fig. 4a), which was associated with a strong increase in inter-TAD interactions in T-ALL. Furthermore, the TAD fusion was associated with CTCF changes. We confirmed CTCF binding at the TAD boundary in T cells and an almost complete absence of binding across the T-ALL samples (Fig. 4b and Extended Data Fig. 5a). The absence of CTCF binding was due neither to genomic mutations (Extended Data Fig. 5b) nor to DNA hypermethylation within or adjacent to the CTCF-binding site in T-ALL (data not shown). Furthermore, 5-azacytidine treatment leading to global DNA demethylation led to no restoration of CTCF binding in CUTLL1 cells (Extended Data Fig. 5c). Instead, assay for transposase-accessible chromatin using sequencing (ATAC-seq) data indicated significantly reduced chromatin accessibility of the CTCF-binding site in T-ALL (Fig. 4b and Extended Data Fig. 5d).

In T-ALL, *MYC* transcription is controlled by distant 3D interactions with a long stretch of enhancers, including the previously characterized NOTCH1-bound N-Me/NDME element^{37,38} (Fig. 4b). As a result of the TAD fusion, the *MYC* promoter and the

Fig. 4 | CTCF-mediated TAD insulation defines the accessibility of MYC promoter-super-enhancer looping. **a**, The top row shows Hi-C interaction heat maps, with the *MYC* locus and super-enhancers indicated. The second row shows heat maps of per-bin \log_2 (fold change) in interactions when compared to the T cell 1 sample. **b**, CTCF and H3K27ac ChIP-seq tracks for the *MYC* locus. CTCF orientation is shown for canonical CTCF binding motifs derived from PWMScan⁶¹ (database JASPAR CORE vertebrates; filtered by $P < 1 \times 10^{-5}$; $n = 143,164$ total CTCF binding motifs). ChIP-seq and ATAC-seq tracks show fold enrichment over input where applicable and counts per million reads otherwise. The gray area indicates super-enhancer elements. Number of replicates: T cells CTCF, $n = 2$; T-ALL 1 CTCF, $n = 2$; T-ALL 3 CTCF, $n = 1$; CUTLL1 CTCF, $n = 5$; Jurkat CTCF, $n = 2$; T cells H3K27ac, $n = 2$; CUTLL1 H3K27ac, $n = 2$; CUTLL1 NOTCH1, $n = 1$; T cells ATAC-seq, $n = 6$; Jurkat ATAC-seq, $n = 3$. **c**, 4C-seq using the *MYC* promoter as the viewpoint. The positive y axis shows interactions with the *MYC* promoter viewpoint as normalized read counts, and the negative y axis shows the significance of differential interactions between T cells and CUTLL1 cells as the \log_{10} (P value) derived by using the edgeR function glmQLFTest. Tracks below are H3K27ac ChIP-seq tracks for T cells and CUTLL1 cells shown as fold enrichment over input. The gray areas indicate super-enhancer elements. Number of replicates: T cells 4C, $n = 2$; CUTLL1 4C, $n = 5$; T cells H3K27ac, $n = 2$; CUTLL1 H3K27ac, $n = 2$. **d**, *MYC* expression shown as \log_2 (FPKM) for T cells ($n = 13$) and T-ALL ($n = 6$). Statistical evaluation was performed by two-sided edgeR analysis with glmQLFTest followed by multiple-testing correction. **e**, Left, distance between the *MYC* promoter and the center enhancer element (MYC-CCE) measured by DNA FISH analysis. The statistical difference between distributions of probe distances was calculated by two-sample one-sided Kolmogorov-Smirnov test following the hypothesis of increased probe distance in T cells when compared to T-ALL. Error bars, s.d.; the center values correspond to the median. Probe pairs: T cells, 993; CUTLL1, 2,001. Median distance: T cells, 412.84 μm; CUTLL1, 264.28 μm. Right, representative images of *MYC* promoter and MYC-CCE probes in T cells and CUTLL1. Box-plot information can be found in the Source Data.

super-enhancer, separated by strong insulation in T cells, were in spatial proximity within the same TAD in leukemic samples (Fig. 4a,b). Circularized chromatin conformation capture and sequencing (4C-seq) analysis using the *MYC* promoter as the

viewpoint confirmed the interaction between the *MYC* promoter and the super-enhancer in primary T-ALL samples and CUTLL1 cells, whereas in untransformed T cells no such interaction was observed (Fig. 4c and Extended Data Fig. 6a). Interestingly, our



analysis showed that the strongest and most significant interactions specifically overlapped with H3K27ac ChIP-seq peaks throughout the entire super-enhancer, including an uncharacterized putative center enhancer element (from this point on referred to as MYC-CEE) and the recently identified BDME/BENC enhancer (Fig. 4c and Extended Data Fig. 6a)^{39,40}. In agreement with our 3D chromosomal interaction data, *MYC* was overexpressed in our cohort of samples from individuals with T-ALL as compared to normal T cells (Fig. 4d). We independently validated the interaction by using 3D FISH with probes targeting the *MYC* promoter and MYC-CEE. Inter-probe distance was significantly higher in T cells than in T-ALL (CUTLL1 cell line), in line with the 4C-seq results (Fig. 4e). Additionally, disruption of CTCF binding by CRISPR-induced mutation in normal T cells significantly reduced interactions between the *MYC* promoter and the CTCF-bound TAD boundary region in edited T cells as compared to wild-type T cells (Extended Data Fig. 7a–e and Supplementary Note).

Pharmacological NOTCH1 inhibition leads to a decrease in 3D interactions in a subset of NOTCH1-regulated loci. Our analysis revealed widespread changes in global TAD structure and intra-TAD activity affecting important genes in T-ALL. However, whether oncogenic drivers, such as NOTCH1, have a direct role in these changes and whether their inhibition can reverse these changes remain open questions. To address this, we performed *in situ* Hi-C in CUTLL1 cells treated with γ SI for 72 h (refs. 21,35). γ SI selectively inhibits NOTCH1 signaling and has strong antileukemic effects^{36,41}. Hi-C analysis after γ SI treatment did not reveal any significant changes in intra-TAD activity (Extended Data Fig. 8a) or reversal of changes in TAD boundary insulation (Extended Data Fig. 8b). Moreover, it was previously shown that about 90% of NOTCH1-binding sites that are sensitive to γ SI treatment (dynamic NOTCH1 sites) are located in putative enhancers. These dynamic NOTCH1-occupied enhancers also show significant changes in H3K27ac signal after NOTCH1 inhibition²¹. We investigated whether chromatin interactions between such enhancers and target promoters were altered after γ SI treatment. We first profiled H3K27ac after γ SI treatment and categorized all non-promoter H3K27ac peaks as either stable peaks or peaks that displayed a significant reduction or increase in H3K27ac signal (Fig. 5a). As previously observed, the H3K27ac peaks with reduced signal after γ SI treatment were significantly enriched for dynamic NOTCH1 binding as compared to stable peaks and those with increased H3K27ac signal²¹ (Fig. 5b).

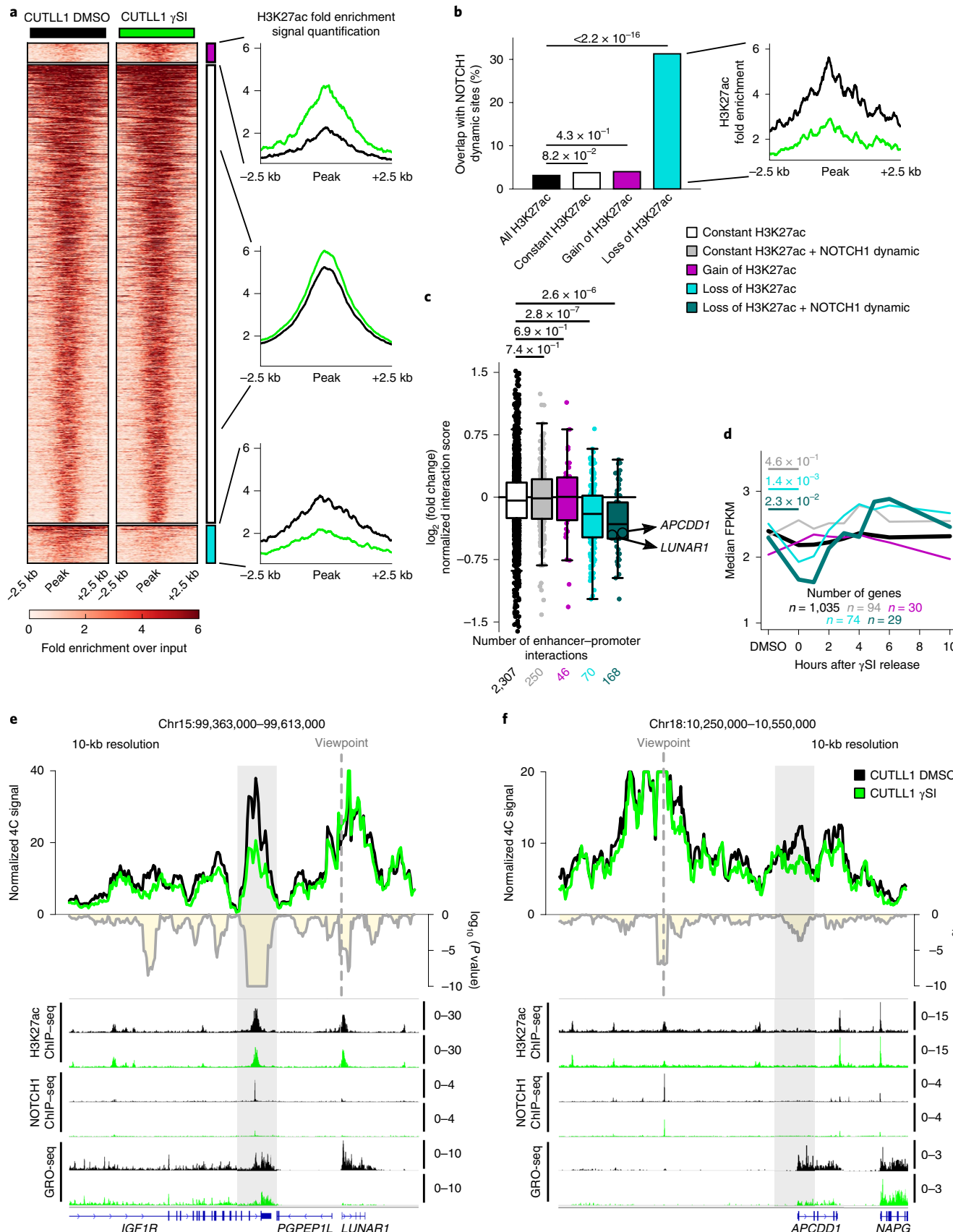
Next, to connect NOTCH1 inhibition, changes in H3K27ac and 3D looping, we used Hi-C data after γ SI treatment to quantify changes in chromatin interactions of H3K27ac-enriched chromatin loops identified by H3K27ac HiChIP in CUTLL1 cells⁴². Our HiChIP data showed enrichment of enhancer–promoter interactions, as demonstrated by virtual 4C analysis using the *MYC* promoter as the virtual viewpoint (Extended Data Fig. 8c). Dynamic NOTCH1-bound enhancers with reduced H3K27ac levels after γ SI treatment showed the strongest loss of chromatin interactions with connected genes (Fig. 5c). Interestingly, dynamic NOTCH1-bound enhancers with stable H3K27ac signal remained in stable contact with nearby promoters. To correlate changes in chromatin interactions with the dynamics of NOTCH1-dependent transcription, we performed global run-on sequencing (GRO-seq)⁴³ to measure nascent transcription after γ SI treatment and after inhibitor ‘washout’. Interestingly, the enhancer–promoter contacts most sensitive to γ SI treatment included genes that showed significant response in transcription to NOTCH1 inhibition and after γ SI washout (Fig. 5d).

To further validate changes among NOTCH1-sensitive enhancer–promoter interactions, we performed 4C-seq on two previously characterized NOTCH1 T-ALL targets, *LUNAR1* and *APCDD1*. *LUNAR1* is a long noncoding RNA that we have previously identified as a *cis* regulator of expression of the neighboring *IGF1R* gene, achieved by looping of the *LUNAR1* promoter with an *IGF1R* intronic enhancer^{44,45}. 4C-seq using the *LUNAR1* promoter as the viewpoint identified strong interactions with the *IGF1R* enhancer. However, the interactions decreased significantly after NOTCH1 inhibition (Fig. 5e and Extended Data Fig. 8d), which correlated with reduced H3K27ac signal at the enhancer and decreased expression of *LUNAR1* (Fig. 5e and Extended Data Fig. 8d). Similarly, by using 4C-seq with an *APCDD1* enhancer as the viewpoint, which displayed dynamic NOTCH1 binding and reduced H3K27ac signal upon NOTCH1 inhibition, we identified decreased interaction between the enhancer and the promoter of *APCDD1* after γ SI treatment. These changes correlated with reduced expression of *APCDD1* (Fig. 5f and Extended Data Fig. 8e). These results suggest that pharmacological NOTCH1 inhibition can affect the activity (as defined by H3K27ac levels) of dynamic NOTCH1-bound enhancers and that 3D interactions with such enhancers are significantly diminished. However, a subset of NOTCH1-regulated loci had neither significant H3K27ac loss nor reduced chromatin interactions after γ SI treatment, including the previously described *MYC* enhancer–promoter interaction and looping of a dynamic

Fig. 5 | NOTCH1 inhibition affects enhancer–promoter looping, specifically of NOTCH1-dependent enhancers. **a**, H3K27ac occupancy in CUTLL1 cells with and without the NOTCH1 inhibitor γ SI. Groups consisted of stable (middle, white; $n=2,949$), increased (top, purple; $n=125$) and reduced (bottom, light blue; $n=243$) non-promoter H3K27ac signal. The heat map shows the H3K27ac signal as fold enrichment over input, and line plots depict quantification of H3K27ac signal (both created with DeepTools⁶²). Differential analysis was performed with the R package DiffBind using the edgeR method, and differential peaks were selected by $FDR < 0.05$ and $\log_2(\text{fold change}) > 1.0$ or < -1.0 . Number of replicates: CUTLL1 DMSO, $n=4$; CUTLL1 γ SI, $n=2$. **b**, Left, overlap of constant, increased and reduced H3K27ac peaks with previously defined NOTCH1 dynamic sites²¹. Right, quantification of H3K27ac signal shown as fold enrichment over input for peaks with reduced H3K27ac signal and dynamic NOTCH1 binding ($n=76$). Statistical evaluation was performed by two-sided Fisher’s test against all noncoding H3K27ac peaks overlapping dynamic NOTCH1 binding. **c**, Changes in chromatin interactions upon γ SI treatment between non-promoter H3K27ac peaks defined in **a** and **b** and connected gene promoters, shown as $\log_2(\text{fold change})$ in average normalized interaction score (average of $n=2$ biological replicates). Each dot represents an enhancer–promoter interaction defined by H3K27ac HiChIP in CUTLL1 cells. The significance of shifts in interaction strength in comparison to the enhancer–promoter loops of stable enhancers was calculated by unpaired one-sided t test, following the hypothesis of a positive correlation between enhancer activity and promoter looping. **d**, Gene expression upon γ SI treatment for all genes defined in **c**, shown as the $\log_2(\text{fold change})$ in FPKM calculated from GRO-seq data. The significance of differences compared to genes associated with stable H3K27ac signal was calculated by unpaired one-sided t test, following the hypothesis of a positive correlation between enhancer–promoter looping and gene expression. **e,f**, 4C-seq using the *LUNAR1* promoter (**e**) and the *APCDD1* enhancer (**f**) as the viewpoint. The positive y axis shows interactions with the viewpoint as normalized read counts, and the negative y axis shows the significance of differential interactions between untreated and γ SI-treated CUTLL1 cells as the $\log_{10}(P \text{ value})$ calculated with the edgeR function glmQLFTest. Tracks below show H3K27ac and NOTCH1 ChIP-seq and GRO-seq (positive strand only) as fold enrichment over input where applicable and counts per million otherwise. The gray areas indicate *LUNAR1* enhancer (**e**) or *APCDD1* promoter (**f**). Number of replicates: CUTLL1 DMSO 4C *LUNAR1*, $n=2$; CUTLL1 γ SI 4C *LUNAR1*, $n=2$; CUTLL1 DMSO 4C *APCDD1*, $n=2$; CUTLL1 γ SI 4C *APCDD1*, $n=2$; CUTLL1 DMSO H3K27ac, $n=2$; CUTLL1 γ SI H3K27ac, $n=2$; CUTLL1 DMSO NOTCH1, $n=1$; CUTLL1 γ SI NOTCH1, $n=1$; CUTLL1 DMSO GRO-seq, $n=2$; CUTLL1 γ SI GRO-seq, $n=2$. Box-plot information can be found in the Source Data.

NOTCH1-bound enhancer to the *IKZF2* promoter (Extended Data Figs. 8f,g and 9, and Supplementary Note). This suggests that NOTCH1 binding is critical for maintaining enhancer–promoter

contacts in only a subset of loops and additional chromatin regulators may have a role in maintaining the chromatin interactions of γ SI-insensitive loops.



CDK7 inhibition targets γ SI-insensitive enhancer–promoter loops. To further understand the differential sensitivity of dynamic NOTCH1-bound enhancers, we performed a differential binding analysis using LOLA and its associated LOLA database⁴⁶ comparing the γ SI-sensitive and γ SI-insensitive enhancers. Among the chromatin regulators and transcription factors available for T-ALL, we found cyclin-dependent kinase 7 (CDK7) binding to be significantly enriched in γ SI-insensitive enhancers as compared to γ SI-sensitive enhancers (Fig. 6a). To globally assess the role of CDK7 binding in the maintenance of γ SI-insensitive enhancer–promoter loops, we performed Hi-C in CUTLL1 cells treated with the CDK7 inhibitor THZ1, which was previously demonstrated to have strong antileukemic activity⁴⁷. As before, we profiled H3K27ac levels after THZ1 treatment by ChIP-seq and categorized all non-promoter H3K27ac peaks as peaks with stable, significantly reduced (THZ1-lost enhancers) or significantly increased (THZ1-gained enhancers) H3K27ac signal (Fig. 6b). Globally, as previously observed in γ SI treatment, enhancers with significant reduction in H3K27ac signal had a correlative reduction in long-range chromatin interactions to target promoters, whereas THZ1-insensitive enhancers neither gained nor lost chromatin interactions on average (Fig. 6c).

To further test the role of CDK7 in maintaining loops, we performed 4C-seq after THZ1 treatment in the previously identified γ SI-insensitive *MYC* and *IKZF2* loci. We observed a significant decrease in the interaction of both N-Me/NDME and MYC-CEE with the *MYC* promoter after treatment with the CDK7 inhibitor (Fig. 6d and Extended Data Fig. 10a). These changes were accompanied by a significant decrease in H3K27ac signal and *MYC* expression (Fig. 6d and Extended Data Fig. 10a,b). Finally, no significant gain in the binding of CTCF to the TAD boundary was observed, suggesting that the described loss of enhancer–promoter interaction occurs independently of CTCF binding (Extended Data Fig. 10c). Additionally, DNA FISH analysis confirmed a significant increase in 3D distance between *MYC* promoter and MYC-CEE probes after THZ1 treatment (Extended Data Fig. 10d). The effect of CDK7 on DNA looping was further confirmed in another T-ALL cell line and locus (Supplementary Note, Fig. 6e and Extended Data Fig. 10e–g). Overall, we demonstrate that targeting a transcription factor (NOTCH1) affects only a subset of 3D enhancer–promoter interactions associated with dynamic NOTCH1 binding. Additional factors such as CDK7 can maintain contacts in a subset of γ SI-insensitive enhancers in T-ALL. Furthermore, changes in H3K27ac levels emerge as a reliable indicator of chromatin interaction dynamics after drug treatments.

Discussion

Despite the intense focus on the regulatory role of TADs in human disease, it remains largely unexplored whether TAD boundary or intra-TAD activity changes are important for tumor initiation

or maintenance. Indeed, aberrant activation of cancer drivers by enhancer hijacking remains the primary known mechanism linking 3D structural changes to oncogenic transformation^{2,3,48,49}. Our studies further these findings by using human T-ALL as a model. They highlight the underlying complexity of factors regulating the 3D landscape in human leukemia, with notable variations among different leukemia subtypes, and suggest that drugs with reported antileukemic activity partially reverse 3D interactions in specific loci, potentially accounting for the antileukemogenic effects of these drugs.

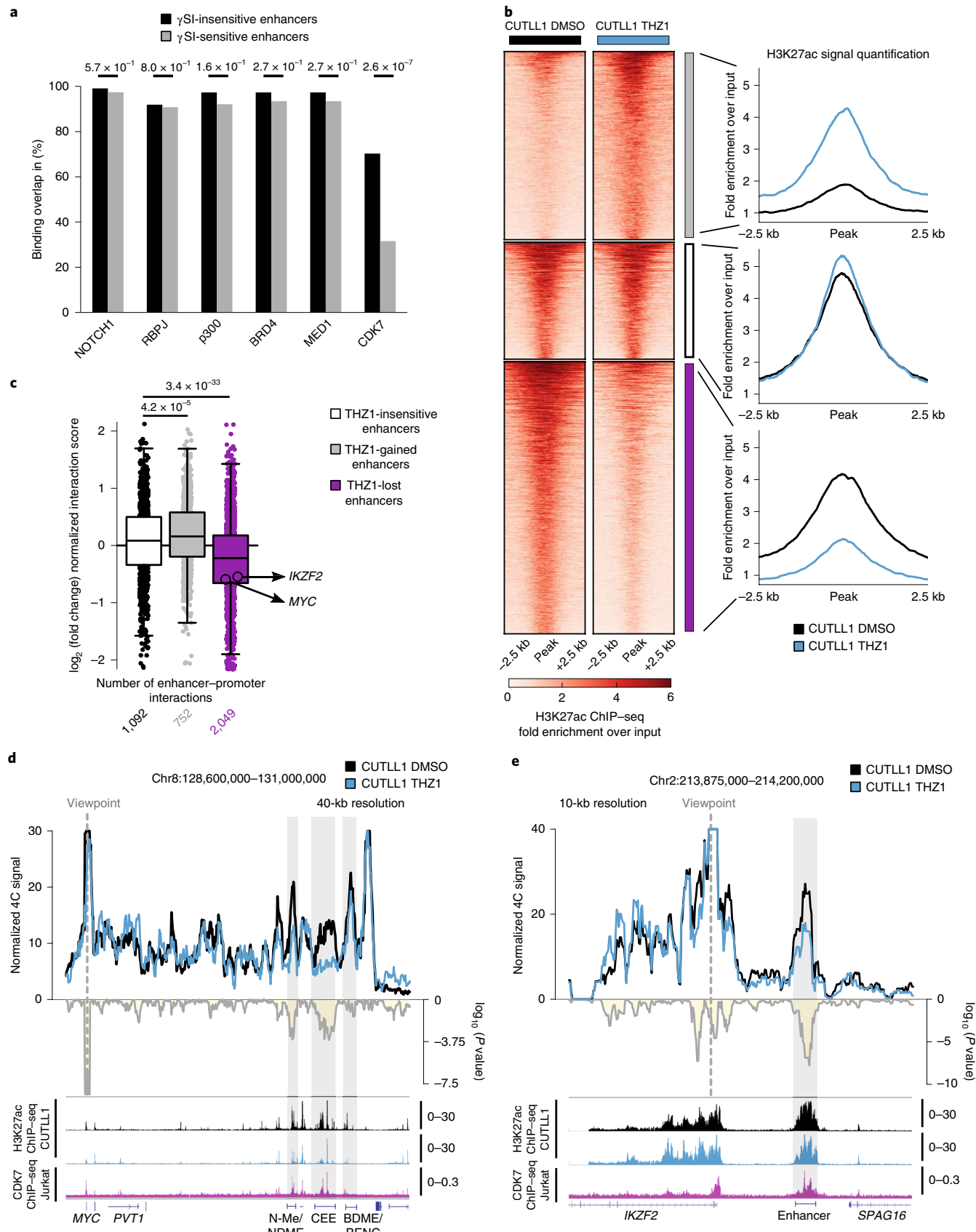
Frequent loss of TAD boundary insulation has previously been observed in human cancer, including in T-ALL⁴⁹. In line with these findings, we identify here a TAD boundary change within the *MYC* locus that is associated with increased enhancer–promoter interactions. *MYC* is an important downstream target of NOTCH1 that activates anabolic pathways to sustain the proliferation induced by constitutive NOTCH1 activation^{35,36}. Our observations suggest that *MYC* upregulation in T-ALL relative to mature T cells is associated with differences in local chromatin architecture. At this point, it is not clear what regulates CTCF binding within the TAD boundary in T-ALL and T cells, although our preliminary studies have excluded a role for DNA methylation and somatic mutations in the CTCF motif. Interestingly, by using ATAC-seq, we found that the CTCF site was accessible in T cells but displayed greatly reduced accessibility in T-ALL, suggesting differential chromatin accessibility as a potential mechanism of regulating CTCF binding. In support of this hypothesis, a recent report identified chromatin accessibility as correlating with CTCF binding during the transition from interphase to prometaphase⁵⁰. In addition to the lost CTCF boundary in T-ALL, we also observed an increase in CTCF binding with the same orientation (facing into the TAD and toward *MYC*) downstream of the super-enhancer. Such clusters of CTCF surrounding super-enhancers have recently been described as super-anchors that ensure super-enhancer-mediated regulation of nearby genes⁵¹. Further studies of the regulatory mechanism underlying CTCF binding and chromatin accessibility in the *MYC* locus could provide alternate strategies to decrease *MYC* expression in T-ALL⁵².

In addition to TAD boundary changes, we also found prevalent intra-TAD activity differences between T-ALL and T cells, as well as between the two subtypes of T-ALL. The changes in intra-TAD activity correlated with expression changes, super-enhancer activity, NOTCH1 binding and insulation mediated by CTCF binding at these TAD boundaries, which appeared to be independent of compartment shifts. Supporting a prominent role for intra-TAD activity changes in modulating gene expression, recent studies tracking 3D chromatin modifications during developmental processes such as embryonic stem cell differentiation and neural development identified significant changes in interactions within (sub-)TADs that correlated with transcriptional levels and epigenetic states^{53,54}. Furthermore, in line with our findings, negative correlations of

Fig. 6 | CDK7 inhibition concomitantly reduces H3K27ac levels and associated enhancer–promoter looping. **a**, LOLA analysis of public ChIP-seq data for CUTLL1 and Jurkat cells in the LOLA database for γ SI-insensitive and γ SI-sensitive enhancers. Statistical differences in overlap of γ SI-insensitive and γ SI-sensitive enhancers with ChIP-seq peaks were calculated by two-sided Fisher's exact test. **b**, H3K27ac occupancy in CUTLL1 cells. Groups consisted of stable (middle, white; $n=1,396$), increased (top, gray; $n=2,246$) and reduced (bottom, purple; $n=3,248$) non-promoter H3K27ac signal. The heat map shows the H3K27ac signal as fold enrichment over input, and line plots depict quantification of H3K27ac signal. Differential analysis was performed with the R package DiffBind using the edgeR method, and differential peaks were selected by $\text{FDR} < 0.05$ and $\log_2(\text{fold change}) > 1.0$ or < -1.0 . Number of replicates: CUTLL1 DMSO, $n=4$; CUTLL1 THZ1, $n=2$. **c**, Changes in Hi-C interactions between the non-promoter H3K27ac peaks defined in **b** and connected gene promoters (defined by CUTLL1 H3K27ac ChIP), shown as the $\log_2(\text{fold change})$ (average of $n=2$ replicates). Each dot represents an enhancer–promoter interaction. The significance of shifts in comparison to enhancer–promoter interactions associated with stable enhancers was calculated by unpaired one-sided t test. **d,e**, 4C-seq using the *MYC* (**d**) and *IKZF2* (**e**) promoter as the viewpoint. The positive y axis shows interactions with the viewpoint as normalized read counts, and the negative y axis shows the significance of differential interactions as $\log_{10}(P \text{ value})$ calculated with the edgeR function glmQLFTest. Tracks below show H3K27ac and CDK7 ChIP-seq tracks and represent fold enrichment over input where applicable and counts per million reads otherwise. The gray areas indicate *MYC* super-enhancer elements (**d**) or *IKZF2* enhancer (**e**). Number of replicates: CUTLL1 DMSO 4C *MYC*, $n=3$; CUTLL1 THZ1 4C *MYC*, $n=3$; CUTLL1 DMSO 4C *IKZF2*, $n=3$; CUTLL1 THZ1 4C *IKZF2*, $n=3$; CUTLL1 DMSO H3K27ac, $n=2$; CUTLL1 THZ1 H3K27ac, $n=2$; Jurkat CDK7, $n=1$. Box-plot information can be found in the Source Data.

intra-TAD interactions with repressive histone marks have been reported in *EZH2*-mutant lymphomas⁵⁵. Herein our observations suggest that gene expression changes in cancer cells are frequently

associated with correlative changes in intra-TAD activity, CTCF insulation and enhancer activity. On a cautionary note, precise identification of 3D chromatin architectural changes in cancer cells



depends on comparison with the respective cell-of-origin population. Although the cell of origin of each of our T-ALL samples is unknown, pilot experiments comparing the 3D chromatin architecture of T-ALL cells to that of human thymic (CD4⁺CD8⁺) progenitors from healthy donors identified similar intra-TAD activity differences specific to T-ALL (data not shown). Further studies are required to understand a possible correlation between the cell of origin and leukemia and to even address potential 3D landscape differences between individual leukemia samples.

Finally, we also addressed the role of oncogenic NOTCH1 in organizing the 3D chromosomal landscape associated with T-ALL transformation and to what extent changes can be reversed by inhibiting NOTCH signaling. NOTCH signaling inhibition is a powerful means to inhibit growth of NOTCH1-induced T-ALL^{41,56}. The effects of γSI have been reported to be selective to dynamic NOTCH1 sites, which are predominantly located within enhancers^{21,38}. Dynamic NOTCH1 sites are also associated with a decrease in enhancer activity after γSI treatment. These findings prompted us to further investigate the impact of NOTCH1 inhibition on remodeling of the 3D landscape in leukemia. Our studies showed that NOTCH1 inhibition using γSI had no effect on global 3D chromatin structure but targeted enhancer–promoter interactions in selected NOTCH1-regulated loci. More specifically, we identified enhancer–promoter loops of dynamic NOTCH1-bound enhancers also associated with a decrease in H3K27ac after γSI treatment that were particularly sensitive to NOTCH1 inhibition. These results concur with a recent report that demonstrated a role for NOTCH1 in facilitating specific long-range interactions in triple-negative breast cancer and mantle cell lymphoma¹⁸.

In an attempt to further understand the importance of NOTCH1 binding in maintaining certain enhancer–promoter loops but not others, we initially found that the enhancers most sensitive to NOTCH1 inhibition tended to be shorter in length. The longer stretch of ‘insensitive’ enhancers might enable other factors to bind and/or keep the chromatin in an open and accessible state for long-range chromatin interactions⁵⁷, thus offering a potential explanation for the variance in enhancer–promoter looping changes we observed for NOTCH1 targets, including *MYC*, *IKZF2*, *APCDD1* and *LUNAR1*. In agreement with this hypothesis, we found enrichment for CDK7 binding in γSI-insensitive enhancers relative to γSI-sensitive enhancers. CDK7 is a kinase previously shown to control the function of RNA polymerase II-mediated transcription⁵⁸. CDK7 inhibition has been shown to have significant effects in hematological malignancies and other cancer types^{47,59,60}. We here showed that pharmacological inhibition of CDK7 in T-ALL by THZ1 resulted in a widespread decrease in enhancer activity as quantified by H3K27ac levels. Enhancers with strong reduction of H3K27ac were also associated with a significant decrease in enhancer–promoter contacts, including the γSI-insensitive loci for *MYC* and *IKZF2*. This clearly highlights the complexity of super-enhancer activity and the factors that dictate super-enhancer interactions with gene promoters. Overall, our study underscores the need for further investigation of factors that maintain or rewire 3D chromosomal interactions, especially during cellular transformation, as they could be potential targets for small-molecule drug development.

Online content

Any methods, additional references, Nature Research reporting summaries, source data, extended data, supplementary information, acknowledgements, peer review information; details of author contributions and competing interests; and statements of data and code availability are available at <https://doi.org/10.1038/s41588-020-0602-9>.

Received: 13 June 2018; Accepted: 25 February 2020;
Published online: 23 March 2020

References

1. Lupiáñez, D. G. et al. Disruptions of topological chromatin domains cause pathogenic rewiring of gene–enhancer interactions. *Cell* **161**, 1012–1025 (2015).
2. Flavahan, W. A. et al. Insulator dysfunction and oncogene activation in *IDH* mutant gliomas. *Nature* **529**, 110–114 (2016).
3. Spielmann, M., Lupiáñez, D. G. & Mundlos, S. Structural variation in the 3D genome. *Nat. Rev. Genet.* **19**, 453–467 (2018).
4. Dekker, J. & Mirny, L. The 3D genome as moderator of chromosomal communication. *Cell* **164**, 1110–1121 (2016).
5. Lieberman-Aiden, E. et al. Comprehensive mapping of long-range interactions reveals folding principles of the human genome. *Science* **326**, 289–293 (2009).
6. Dixon, J. R. et al. Topological domains in mammalian genomes identified by analysis of chromatin interactions. *Nature* **485**, 376–380 (2012).
7. Nora, E. P. et al. Spatial partitioning of the regulatory landscape of the X-inactivation centre. *Nature* **485**, 381–385 (2012).
8. Hnisz, D. et al. Super-enhancers in the control of cell identity and disease. *Cell* **155**, 934–947 (2013).
9. Whyte, W. A. et al. Master transcription factors and Mediator establish super-enhancers at key cell identity genes. *Cell* **153**, 307–319 (2013).
10. Gong, Y. et al. Stratification of TAD boundaries reveals preferential insulation of super-enhancers by strong boundaries. *Nat. Commun.* **9**, 542 (2018).
11. Ong, C. T. & Corces, V. G. CTCF: an architectural protein bridging genome topology and function. *Nat. Rev. Genet.* **15**, 234–246 (2014).
12. Hnisz, D., Day, D. S. & Young, R. A. Insulated neighborhoods: structural and functional units of mammalian gene control. *Cell* **167**, 1188–1200 (2016).
13. Nora, E. P. et al. Targeted degradation of CTCF decouples local insulation of chromosome domains from genomic compartmentalization. *Cell* **169**, 930–944 (2017).
14. Rao, S. S. P. et al. Cohesin loss eliminates all loop domains. *Cell* **171**, 305–320 (2017).
15. Guo, Y. et al. CRISPR inversion of CTCF sites alters genome topology and enhancer/promoter function. *Cell* **162**, 900–910 (2015).
16. Narendra, V. et al. CTCF establishes discrete functional chromatin domains at the *Hox* clusters during differentiation. *Science* **347**, 1017–1021 (2015).
17. Weischenfeldt, J. et al. Pan-cancer analysis of somatic copy-number alterations implicates *IRS4* and *IGF2* in enhancer hijacking. *Nat. Genet.* **49**, 65–74 (2017).
18. Petrovic, J. et al. Oncogenic Notch promotes long-range regulatory interactions within hyperconnected 3D cliques. *Mol. Cell* **73**, 1174–1190 (2019).
19. Grabher, C., von Boehmer, H. & Look, A. T. Notch 1 activation in the molecular pathogenesis of T-cell acute lymphoblastic leukaemia. *Nat. Rev. Cancer* **6**, 347–359 (2006).
20. Belver, L. & Ferrando, A. The genetics and mechanisms of T cell acute lymphoblastic leukaemia. *Nat. Rev. Cancer* **16**, 494–507 (2016).
21. Wang, H. et al. NOTCH1–RBPJ complexes drive target gene expression through dynamic interactions with superenhancers. *Proc. Natl. Acad. Sci. USA* **111**, 705–710 (2014).
22. Hunger, S. P. & Mullighan, C. G. Acute lymphoblastic leukemia in children. *N. Engl. J. Med.* **373**, 1541–1552 (2015).
23. Weng, A. P. et al. Activating mutations of *NOTCH1* in human T cell acute lymphoblastic leukemia. *Science* **306**, 269–271 (2004).
24. Liu, Y. et al. The genomic landscape of pediatric and young adult T-lineage acute lymphoblastic leukemia. *Nat. Genet.* **49**, 1211–1218 (2017).
25. Coustan-Smith, E. et al. Early T-cell precursor leukaemia: a subtype of very high-risk acute lymphoblastic leukaemia. *Lancet Oncol.* **10**, 147–156 (2009).
26. Zhang, J. et al. The genetic basis of early T-cell precursor acute lymphoblastic leukaemia. *Nature* **481**, 157–163 (2012).
27. Palomero, T. et al. CUTLL1, a novel human T-cell lymphoma cell line with t(7;9) rearrangement, aberrant NOTCH1 activation and high sensitivity to γ-secretase inhibitors. *Leukemia* **20**, 1279–1287 (2006).
28. Sulis, M. L. et al. NOTCH1 extracellular juxtamembrane expansion mutations in T-ALL. *Blood* **112**, 733–740 (2008).
29. Lazaris, C., Kelly, S., Ntziachristos, P., Aifantis, I. & Tsirigos, A. HiC-bench: comprehensive and reproducible Hi-C data analysis designed for parameter exploration and benchmarking. *BMC Genomics* **18**, 22 (2017).
30. Kourtis, N. et al. Oncogenic hijacking of the stress response machinery in T cell acute lymphoblastic leukemia. *Nat. Med.* **24**, 1157–1166 (2018).
31. Yang, T. et al. HiCRep: assessing the reproducibility of Hi-C data using a stratum-adjusted correlation coefficient. *Genome Res.* **27**, 1939–1949 (2017).
32. Zhang, Z. et al. Expression of a non-DNA-binding isoform of Helios induces T-cell lymphoma in mice. *Blood* **109**, 2190–2197 (2007).
33. Vilimas, T. et al. Targeting the NF-κB signaling pathway in Notch1-induced T-cell leukemia. *Nat. Med.* **13**, 70–77 (2007).
34. Espinosa, L. et al. The Notch/Hes1 pathway sustains NF-κB activation through CYLD repression in T cell leukemia. *Cancer Cell* **18**, 268–281 (2010).
35. Weng, A. P. et al. c-Myc is an important direct target of Notch1 in T-cell acute lymphoblastic leukemia/lymphoma. *Genes Dev.* **20**, 2096–2109 (2006).

36. Palomero, T. et al. NOTCH1 directly regulates *c-MYC* and activates a feed-forward-loop transcriptional network promoting leukemic cell growth. *Proc. Natl Acad. Sci. USA* **103**, 18261–18266 (2006).
37. Herranz, D. et al. A NOTCH1-driven *MYC* enhancer promotes T cell development, transformation and acute lymphoblastic leukemia. *Nat. Med.* **20**, 1130–1137 (2014).
38. Yashiro-Ohtani, Y. et al. Long-range enhancer activity determines *Myc* sensitivity to Notch inhibitors in T cell leukemia. *Proc. Natl Acad. Sci. USA* **111**, E4946–E4953 (2014).
39. Shi, J. et al. Role of SWI/SNF in acute leukemia maintenance and enhancer-mediated *Myc* regulation. *Genes Dev.* **27**, 2648–2662 (2013).
40. Bahr, C. et al. A *Myc* enhancer cluster regulates normal and leukaemic haematopoietic stem cell hierarchies. *Nature* **553**, 515–520 (2018).
41. Deangelo, D. J. et al. A phase I clinical trial of the Notch inhibitor MK-0752 in patients with T-cell acute lymphoblastic leukemia/lymphoma (T-ALL) and other leukemias. *J. Clin. Oncol.* **24**, 6585–6585 (2006).
42. Mumbach, M. R. et al. HiChIP: efficient and sensitive analysis of protein-directed genome architecture. *Nat. Methods* **13**, 919–922 (2016).
43. Hah, N. et al. A rapid, extensive, and transient transcriptional response to estrogen signaling in breast cancer cells. *Cell* **145**, 622–634 (2011).
44. Trimarchi, T. et al. Genome-wide mapping and characterization of Notch-regulated long noncoding RNAs in acute leukemia. *Cell* **158**, 593–606 (2014).
45. Medyout, H. et al. High-level IGF1R expression is required for leukemia-initiating cell activity in T-ALL and is supported by Notch signaling. *J. Exp. Med.* **208**, 1809–1822 (2011).
46. Sheffield, N. C. & Bock, C. LOLA: enrichment analysis for genomic region sets and regulatory elements in R and Bioconductor. *Bioinformatics* **32**, 587–589 (2015).
47. Kwiatkowski, N. et al. Targeting transcription regulation in cancer with a covalent CDK7 inhibitor. *Nature* **511**, 616–620 (2014).
48. Northcott, P. A. et al. Enhancer hijacking activates GFI1 family oncogenes in medulloblastoma. *Nature* **511**, 428–434 (2014).
49. Hnisz, D. et al. Activation of proto-oncogenes by disruption of chromosome neighborhoods. *Science* **351**, 1454–1458 (2016).
50. Oomen, M. E., Hansen, A. S., Liu, Y., Darzacq, X. & Dekker, J. CTCF sites display cell cycle-dependent dynamics in factor binding and nucleosome positioning. *Genome Res.* **29**, 236–249 (2019).
51. Vian, L. et al. The energetics and physiological impact of cohesin extrusion. *Cell* **173**, 1165–1178 (2018).
52. King, B. et al. The ubiquitin ligase FBXW7 modulates leukemia-initiating cell activity by regulating MYC stability. *Cell* **153**, 1552–1566 (2013).
53. Bonev, B. et al. Multiscale 3D genome rewiring during mouse neural development. *Cell* **171**, 557–572 (2017).
54. Dixon, J. R. et al. Chromatin architecture reorganization during stem cell differentiation. *Nature* **518**, 331–336 (2015).
55. Donaldson-Collier, M. C. et al. EZH2 oncogenic mutations drive epigenetic, transcriptional, and structural changes within chromatin domains. *Nat. Genet.* **51**, 517–528 (2019).
56. Bellavia, D., Palermo, R., Felli, M. P., Scarpanti, I. & Checquolo, S. Notch signaling as a therapeutic target for acute lymphoblastic leukemia. *Expert Opin. Ther. Targets* **22**, 331–342 (2018).
57. Siersbaek, R. et al. Transcription factor cooperativity in early adipogenic hotspots and super-enhancers. *Cell Rep.* **7**, 1443–1455 (2014).
58. Laroche, S. et al. Cyclin-dependent kinase control of the initiation-to-elongation switch of RNA polymerase II. *Nat. Struct. Mol. Biol.* **19**, 1108–1115 (2012).
59. Chipumuro, E. et al. CDK7 inhibition suppresses super-enhancer-linked oncogenic transcription in *MYCN*-driven cancer. *Cell* **159**, 1126–1139 (2014).
60. Christensen, C. L. et al. Targeting transcriptional addictions in small cell lung cancer with a covalent CDK7 inhibitor. *Cancer Cell* **26**, 909–922 (2014).
61. Ambrosini, G., Groux, R. & Bucher, P. PWMScan: a fast tool for scanning entire genomes with a position-specific weight matrix. *Bioinformatics* **34**, 2483–2484 (2018).
62. Ramirez, F. et al. deepTools2: a next generation web server for deep-sequencing data analysis. *Nucleic Acids Res.* **44**, W160–W165 (2016).

Publisher's note Springer Nature remains neutral with regard to jurisdictional claims in published maps and institutional affiliations.

© The Author(s), under exclusive licence to Springer Nature America, Inc. 2020

Methods

Cell culture. The CUTLL1 human cell line and Jurkat cells were cultured in RPMI-1640 medium supplemented with 10% FBS, penicillin, streptomycin and glutamine. Naive CD4⁺ T cells were purchased from Lonza and cultured in X-vivo 15 culture medium (Lonza) supplemented with 5% human serum (Gemini Bioproducts) and 10 ng ml⁻¹ human interleukin (IL)-2.

Primary T-ALL samples. Primary samples from individuals with T-ALL were collected by Columbia Presbyterian Hospital or Weill Cornell Medical College with informed consent and approved and analyzed under the supervision of the Columbia University Medical Center Institutional Review Board or the Weill Cornell Medical College Institutional Review Board. For expansion of these cells, 1 × 10⁶ cells were transplanted into immunodeficient NOD-SCID-gamma (NSG) mouse strains via retro-orbital injection, as previously performed⁶³. Cells collected from the spleen of these primary recipients were used for the *in situ* Hi-C experiment. All mouse experiments were performed according to ethical guidelines set by the Institutional Animal Care and Use Committee and New York University.

In situ Hi-C. *In situ* Hi-C was performed as described in Rao et al.⁶⁴. Primary samples were processed as one replicate, and all cell line experiments were processed with two biological replicates. Briefly, 20 million cells were fixed in 1% formaldehyde for 10 min. Fixed cells were permeabilized in 1 ml lysis buffer (10 mM Tris-HCl pH 8, 10 mM NaCl, 0.2% NP-40 and protease inhibitor cocktail (Sigma)) for 15 min on ice and spun down (2,000 g, 5 min, 4°C). Cell pellets were resuspended in 345 µl of 1× NEBuffer2 (NEB) per aliquot of 5 million cells, and 38 µl of 1% SDS was added to each aliquot, followed by incubation at 65°C for 10 min. Then, 43 µl of 10% Triton X-100 was added to quench the SDS. To digest chromatin, 400 U of HindIII (NEB) was added per aliquot and samples were incubated at 37°C overnight with continuous agitation (900 r.p.m.). After digestion, restriction sites were filled in with Klenow (NEB) in the presence of biotin-14-dATP (Life Technologies), dCTP, dGTP and dTTP for 2 h at 37°C. Blunt-end ligation was performed by adding 700 µl of ligation mix (containing 50 U of T4 DNA ligase (Invitrogen)), followed by overnight incubation at 16°C.

Cross-links were reversed by adding 50 µl of 10 mg ml⁻¹ proteinase K (Invitrogen) per aliquot and incubating at 65°C for 2 h, followed by addition of another 50 µl of 10 mg ml⁻¹ proteinase K and incubation overnight. All aliquots for each replicate were pooled, and DNA was extracted by phenol-chloroform extraction protocol. RNA was digested by adding 1 µl of 1 mg ml⁻¹ RNase A (Sigma) and incubating at 37°C for 30 min. Biotin was removed from nonligated restriction fragment ends by incubating 40 µg of DNA with T4 DNA polymerase (NEB) for 4 h at 20°C in the presence of dATP and dGTP. After purification (Amicon Ultra 30K) and sonication (Covaris E220), the DNA was double size selected on AMPure XP beads (Beckman Coulter, 0.8–1.1×). End repair was performed with T4 DNA polymerase (NEB), T4 DNA polynucleotide kinase (NEB), Klenow (NEB) and dNTPs in 1× T4 DNA ligase reaction buffer (NEB), followed by dATP addition with Klenow. Biotin-marked ligation products were isolated with MyOne Streptavidin C1 Dynabeads (Life Technologies). Paired-end adaptors (Illumina) were ligated to DNA fragments by using 15 U of T4 DNA ligase (Invitrogen) for 2 h at room temperature. Bead-bound DNA was amplified with six PCR amplification cycles using PE PCR 1.0 and PE PCR 2.0 primers (Illumina). Primary T-ALL samples 2–5, the sample from T cell donor 2 and the ETP-ALL samples along with the CUTLL1 samples treated with DMSO or THZ1 were processed with the commercial Arima Genomics HiC kit according to the manufacturer's guidelines. The Hi-C libraries were sequenced on the Illumina HiSeq 2500 or 4000 platform at 50 cycles.

4C-seq. For the *LUNAR1* and *APCDD1* viewpoints, we created biological duplicates for all experiments. For the *MYC* viewpoint, we created five biological replicates for CUTLL1 cells treated with DMSO, three replicates for CUTLL1 cells treated with γSI and two replicates for T cells. Experiments with edited T cells were performed with two replicates, and CUTLL1 cells were treated with DMSO or THZ1 in biological triplicate.

For each replicate, 10 million cells were fixed in 2% formaldehyde and 10% FBS in PBS for 10 min at room temperature. For edited and wild-type T cells, 5 million cells were used. Cross-linking was quenched with glycine, and 4C-seq was performed as described previously¹⁰. Cells were lysed on ice with 1 ml lysis buffer (50 mM Tris pH 7.3, 150 mM NaCl, 5 mM EDTA, 0.5% NP-40 and 1% Triton X-100) for 15 min. Nuclei were spun down and resuspended in 360 µl water (or frozen). Then, 60 µl of 10× DpnII restriction buffer was added along with 15 µl of 10% SDS, and samples were left shaking for 1 h at 37°C, followed by addition of 150 µl of 10% Triton X-100 and additional shaking for 1 h at 37°C. Five microliters of undigested control was stored, and nuclei were incubated overnight with 200 U of DpnII restriction enzyme (NEB, R0543M). A fresh 200 U of DpnII was added the following morning, and samples were digested for 6 h. After this, digestion was checked for completion by running 5 µl of sample in a 1% agarose gel. DpnII was inactivated with 80 µl of 10% SDS, and a proximity ligation reaction was performed in a 7-ml volume with 4,000 U of T4 DNA ligase (NEB, M0202M). Cross-links were reversed at 65°C overnight after adding 300 µg proteinase K. Samples were then treated with 300 µg RNase A for 45 min at 37°C, and DNA was ethanol

precipitated. A second restriction digest was performed overnight in a 500-µl reaction with 50 U of Csp6I (Fermentas, ER0211). The enzyme was inactivated at 65°C for 25 min, and a proximity ligation reaction was performed in a 14-ml volume with 6,000 U of T4 DNA ligase. Sample DNA was ethanol precipitated and purified with the QIAquick PCR purification kit (Qiagen). To generate the 4C-seq library, 1 µg of prepared 4C template was amplified with 30 PCR cycles per bait for each condition (see Supplementary Table 6 for viewpoint sequences), and the amplified fragments were sequenced on the Illumina HiSeq 2500 platform to generate single-end reads at 50 cycles.

HiChIP. HiChIP was performed as previously described⁴² with some modifications. In brief, up to 10 million cross-linked cells were resuspended in 500 µl of ice-cold HiC lysis buffer (10 mM Tris-HCl pH 7.5, 10 mM NaCl, 0.2% NP-40 and 1× protease inhibitors) and rotated at 4°C for 30 min. Nuclei were pelleted and washed once with 500 µl of ice-cold HiC lysis buffer. The pellet was then resuspended in 100 µl of 0.5% SDS and incubated at 62°C for 10 min. Then, 285 µl of water and 50 µl of 10% Triton X-100 were added, and samples were rotated at 37°C for 15 min. To this, 50 µl of NEBuffer 2 and 15 µl of 25 U µl⁻¹ MboI restriction enzyme (NEB, R0147) were added, and samples were rotated at 37°C for 2 h. MboI was heat inactivated at 62°C for 20 min. Then, 52 µl of incorporation master mix (37.5 µl of 0.4 mM biotin-dATP (Jena Biosciences, NU-835-BIO14-S), 1.5 µl of a dCTP, dGTP and dTTP mix (10 mM each) and 10 µl of 5 U µl⁻¹ Klenow fragment (NEB, M0210)) was added. Reactions were rotated at 37°C for 1 h, and 948 µl of ligation master mix (150 µl of 10× NEB T4 DNA ligase buffer with 10 mM ATP (NEB, B0202), 125 µl of 10% Triton X-100, 3 µl of 50 mg ml⁻¹ BSA (Thermo Fisher, AM2616), 10 µl of 400 U µl⁻¹ T4 DNA ligase (NEB, M0202) and 660 µl of water) was added. Reactions were rotated at room temperature for 4 h. After proximity ligation, nuclei were pelleted and the supernatant was removed. The nuclear pellet was resuspended in 880 µl of nuclear lysis buffer (50 mM Tris-HCl pH 7.5, 10 mM EDTA, 0.5% SDS and 1× Roche protease inhibitor (11697498001)) and sonicated with a Bioruptor 300 (Diagenode) for eight cycles of 30 s each, on the high setting. Clarified samples were transferred to Eppendorf tubes and diluted 1:5 with ChIP dilution buffer (0.01% SDS, 1.1% Triton X-100, 1.2 mM EDTA, 16.7 mM Tris-HCl pH 7.5 and 167 mM NaCl). Cells were precleared with 30 µl of Protein G Dynabeads (Life Technologies, 10004D) by rotation at 4°C for 1 h. Supernatants were transferred to fresh tubes, and antibody was added (7.5 µg of anti-H3K27ac antibody for 10 million cells). Samples were incubated overnight at 4°C. The next day, 30 µl of Protein G Dynabeads was added and samples were rotated at 4°C for 2 h. After bead capture, beads were washed with low-salt wash buffer (0.1% SDS, 1% Triton X-100, 2 mM EDTA, 20 mM Tris-HCl pH 7.5 and 150 mM NaCl), high-salt wash buffer (0.1% SDS, 1% Triton X-100, 2 mM EDTA, 20 mM Tris-HCl pH 7.5 and 500 mM NaCl) and LiCl wash buffer (10 mM Tris-HCl pH 7.5, 250 mM LiCl, 1% NP-40, 1% sodium deoxycholate and 1 mM EDTA). Samples were eluted with 150 µl of DNA elution buffer (50 mM sodium bicarbonate pH 8.0 and 1% SDS, freshly made) and incubated at 37°C for 30 min with rotation. Supernatant was transferred to a fresh tube, and elution was repeated with another 150 µl of elution buffer. Then, 5 µl of proteinase K (20 mg ml⁻¹; Thermo Fisher) was added to the 300-µl reaction, and samples were incubated overnight at 65°C. Samples were purified with DNA Clean and Concentrator columns (Zymo Research) and eluted in 10 µl of water. Post-ChIP DNA was quantified by Qubit (Thermo Fisher), and 5 µl of Streptavidin C1 beads (Thermo Fisher) was washed with Tween wash buffer (5 mM Tris-HCl pH 7.5, 0.5 mM EDTA, 1 M NaCl and 0.05% Tween-20) and then resuspended in 10 µl of 2× biotin binding buffer (10 mM Tris-HCl pH 7.5, 1 mM EDTA and 2 M NaCl). Beads were added to the samples, which were then incubated at room temperature for 15 min with shaking. After capture, beads were washed twice by adding 150 µl of Tween wash buffer and incubating at 55°C for 2 min with shaking. Samples were then washed in 100 µl of 1× TD buffer (2× TD buffer: 20 mM Tris-HCl pH 7.5, 10 mM MgCl₂ and 20% dimethylformamide). After washes, beads were resuspended in 22 µl of Arima elution buffer, and the library was generated on Streptavidin C1 beads with a modified Kapa Library Preparation kit. End repair and adaptor ligation were carried out on 20 µl of bead-bound DNA. Then, 1 µl of 15 µM Illumina TruSeq sequencing adaptors was added to the sample along with 49 µl of master mix containing DNA ligase, ligase buffer and PCR-grade water, and samples were incubated at 20°C for 15 min. After adaptor ligation, the samples were washed twice with Arima wash buffer and incubated at 55°C for 2 min with shaking. The samples were washed once more with 100 µl of elution buffer and finally resuspended in 22 µl of elution buffer. To each sample, 25 µl of HiFi HotStart Ready Mix and 10× primer mix (Kapa Library Amplification Kit) were added. The following PCR program was performed: 98°C for 45 s followed by ten cycles at 98°C for 15 s, 60°C for 30 s and 72°C for 30 s, with a final extension completed at 72°C for 1 min (cycle number was estimated on the basis of the amount of material from the post-ChIP Qubit reading (approximately 50 ng was run in six cycles, while 25 ng was run in seven cycles, 12.5 ng in eight cycles, etc.). Libraries were sequenced on the Illumina HiSeq 4000 platform on PE50 mode.

In vitro drug treatment. CUTLL1 cells were treated with γSI (Compound E) purchased from Alexis Bioscience at a 1 µM final concentration. Treatment was performed every 12 h for 72 h. THZ1 was purchased from Cayman Chemical (9002215), and cells were treated at a 100 nM final concentration every

12 h for 24 h. For 5-azacytidine, cells were treated with a 100 nM concentration every day for 3 d (72 h).

GRO-seq and library preparation. GRO-seq was performed in CUTLL1 cells treated with either DMSO or γ SI at a 1 μ M concentration for 72 h. All experiments were performed in biological duplicate. GRO-seq sample preparation was performed as described previously⁴⁵. Briefly, nuclei were isolated in swelling buffer (10 mM Tris-HCl pH 7.5, 2 mM MgCl₂ and 3 mM CaCl₂), lysed twice in lysis buffer (10 mM Tris-HCl pH 7.5, 2 mM MgCl₂, 3 mM CaCl₂, 10% glycerol and 0.5% NP-40) and snap frozen in freezing buffer (50 mM Tris pH 8.0, 40% glycerol, 5 mM MgCl₂, and 0.1 mM EDTA). For the run-on reaction, an equal volume of reaction buffer was added to thawed nuclei (10 mM Tris pH 8.0, 5 mM MgCl₂, 300 mM KCl, 500 μ M ATP, 500 μ M GTP, 5 μ M CTP, 500 μ M BrUTP, 1 mM dithiothreitol, 100 U ml⁻¹ SuperaseIN and 1% sarkosyl), and samples were mixed and incubated at 30 °C for 5 min. The reaction was stopped with TRIzol reagent, and RNA was extracted with phenol-chloroform and ethanol precipitated. RNA was heated in fragmentation buffer (40 mM Tris pH 8.0, 100 mM KCl, 6.25 mM MgCl₂ and 1 mM dithiothreitol), treated with DNase and purified with Zymo RNA Clean and Concentrator columns (Zymo Research) by using the >17-nucleotide protocol. Run-on RNA was immunoprecipitated with BSA-blocked BrDU beads (Santa Cruz Biotechnology) in binding buffer (0.5 \times SSPE, 1 mM EDTA and 0.05% Tween-20) for 1 h at 4 °C, washed and eluted in elution buffer (5 mM Tris pH 7.5, 300 mM NaCl, 20 mM dithiothreitol, 1 mM EDTA and 1% SDS) at 65 °C for 20 min. Nascent RNA was further extracted with phenol-chloroform, and sequencing libraries were prepared.

Sanger sequencing of the CTCF-binding site in the MYC locus. Genomic DNA from CUTLL1, Jurkat and T-ALL 1 cells was isolated with the Qiagen DNeasy kit according to the manufacturer's guidelines. The target locus was PCR amplified with Phusion High-Fidelity PCR Master Mix (Thermo Fisher, F531S) using 100 ng of genomic DNA as the template. Primer sequences are listed in Supplementary Table 6. PCR products were purified on Qiagen PCR purification columns and submitted for Sanger sequencing to Genewiz.

CTCF-motif-targeting guide RNA sequence. The guide RNA target sequence was 5'-UCUACAAACAUCCACCAUG-3'. The guide RNA along with the tracer RNA was purchased as a synthetic guide RNA from Synthego with 2'-O-methyl and 3'-phosphorothioate modifications of the first and last three nucleotides.

Editing of T cells. Naive T cells were activated with CD3/CD28 beads from Thermo Fisher Scientific (11161D) for 48 h. After activation, the CD3/CD28 beads were magnetically removed and 2 million activated T cells were transfected by electrotransfer with either ribonucleoprotein complex consisting of 1.5 μ g of Cas9 protein and 1 μ g of guide RNA or 1.5 μ g of Cas9 protein alone for every 200,000 cells using the Neon transfection system at 1,200 V with a width of 40 and one pulse. After electroporation, cells were diluted into culture medium at 10⁶ cells per ml. The electroporation step was repeated after 24 h. Forty-eight hours after the second transfection, genomic DNA was isolated. The target CTCF region was PCR amplified and subjected to Sanger sequencing. Editing efficiency was computed by using the ICE computational program from Synthego.

High-throughput 3D DNA FISH. Generation of FISH probes. Custom FISH probes targeting the *MYC* promoter and enhancer were designed with the SureDesign custom oligonucleotide design tool from Agilent with homology to the regions of interest mined from the hg19 genome build, using the default parameters of the SureDesign tool. The *MYC* promoter probe library targeted a 60-kb region centered on the promoter, whereas the enhancer probe library targeted a 100-kb region including the center enhancer element of the *MYC* super-enhancer cluster.

3D FISH experimental protocol. 3D FISH was performed with the Dako FISH Histology accessory kit from Agilent (K579911-5) according to the manufacturer's guidelines. Briefly, 200,000 cells were cytospun to poly(L-lysine)-treated glass slides at 1,200 r.p.m. for 5 min. Cells were subsequently fixed for 10 min with 4% formaldehyde in PBS at room temperature, followed by membrane permeabilization with 0.5% Triton X-100 in PBS for 20 min at room temperature. Slides were washed once in 1× PBS followed by RNase treatment (100 μ g ml⁻¹ RNase A in 2× SSC buffer). Cells were then washed with 2× SSC and dehydrated through an alcohol series (2×100% ethanol and 2×70% ethanol, 2 min each at room temperature). Slides were washed with 1× Dako wash buffer for 5 min at room temperature and then treated with 1× Dako pretreatment solution at 98 °C for 2 min and allowed to cool for 15 min at room temperature. After pretreatment, slides were washed twice with 1× Dako wash buffer for 3 min each at room temperature. Slides were then treated with cold pepsin at 37 °C for 2 min followed by two washes with 1× Dako wash buffer for 3 min each at room temperature. Slides were then dehydrated through a series of ethanol washes (70%, 80% and 100% ethanol, 2 min each at room temperature). After the ethanol washes, slides were air dried and set up for probe hybridization. For each slide, 1 μ l of each probe mixed with 9 μ l of IQFISH Fast Hybridization buffer was added, and slides were covered with a coverslip and sealed with rubber cement. Slides were incubated at 80 °C in a heat block for 10 min followed by incubation for 90 min in a hot-air

oven set at 45 °C in the dark. After hybridization, the rubber cement was removed and the slides were washed with 1× Dako stringent wash buffer for 5 min at room temperature. This was immediately followed by a second wash with 1× Dako stringent wash buffer for 10 min at 56 °C. The stringent washes were followed by two washes with 1× Dako wash buffer for 3 min each at room temperature. Slides were then dehydrated through a series of ethanol washes (70%, 80% and 100% ethanol, 2 min each at room temperature), air dried and mounted with coverslips using Immune-mount with DAPI stain.

Computational analysis. Raw sequencing data were mostly processed with the hic-bench platform²⁹. Detailed descriptions of individual analyses can be found in the Supplementary Methods.

Further detailed information on experimental design and reagents can be found in the Nature Research Reporting Summary.

Statistics and reproducibility. All sequencing experiments and functional analyses involved at least two replicates that were independently prepared, cultured and treated, including experiments with cell lines (CUTLL1, Jurkat and activated T cells) or xenografts of different primary samples from patients, obtained by using independent recipient mice for each replicate.

Statistical analyses for differential gene expression, differential ChIP-seq peaks and differential 4C-seq peaks were conducted with the R Bioconductor package edgeR using two or more independent replicates as described above (after intra-sample sequencing depth normalization with the 'cpm' function and inter-sample dispersion correction with the 'estimateCommonDisp' and 'estimateTagwiseDisp' functions, followed by 'glmQLFit' and 'glmQLFTest' for differential analysis). Differential Hi-C analysis, based on either compartment scores or TAD activity scores, was performed with two-sided *t* tests.

The statistical significance of differences in odds ratios between two groups (Figs. 2f, 5b and 6a) was calculated by two-sided Fisher's exact test.

When we expected changes in one direction, we used one-tailed *t* tests under the following hypotheses (Fig. 2d,e,g):

H_0 : The mean expression of genes associated with differential intra-TAD activity (for example, expression fold change T-ALL/T-cells in T-ALL-specific TADs) or the mean CTCF binding strength of peaks associated with differential intra-TAD activity is unchanged or has a negative correlation with intra-TAD activity changes.

$$\text{Example : } \mu_{\text{T-ALL-specific TADs}} \leq \mu_{\text{constant TADs}}$$

H_A : The mean expression of genes associated with differential intra-TAD activity (for example, expression fold change T-ALL/T-cells in T-ALL-specific TADs) or the mean CTCF binding strength of peaks associated with differential intra-TAD activity has a positive correlation with intra-TAD activity changes.

$$\text{Example : } \mu_{\text{T-ALL-specific TADs}} > \mu_{\text{constant TADs}}$$

Similarly, for comparisons of enhancer-promoter loops or associated expression of genes connected with enhancers of reduced activity (Figs. 5c,d and 6c), we used one-tailed *t* tests under the following hypotheses:

H_0 : The mean looping strength of enhancer-promoter pairs in treated CUTLL1 cells is greater than or equal to the looping strength of enhancer-promoter pairs in untreated CUTLL1 cells or the mean expression of associated genes in treated CUTLL1 cells is greater than or equal to the expression of associated genes in untreated CUTLL1 cells.

$$\text{Example : } \mu_{\text{treated CUTLL1}} \geq \mu_{\text{untreated CUTLL1}}$$

H_A : The mean looping strength of enhancer-promoter pairs in treated CUTLL1 cells is less than the looping strength of enhancer-promoter pairs in untreated CUTLL1 cells or the mean expression of associated genes in treated CUTLL1 cells is less than the expression of associated genes in untreated CUTLL1 cells.

$$\text{Example : } \mu_{\text{treated CUTLL1}} < \mu_{\text{untreated CUTLL1}}$$

Lastly, for comparisons of 3D FISH probe distances used for validation of genome-wide comparisons (Fig. 4e and Extended Data Fig. 10d), we used one-tailed Kolmogorov-Smirnov tests under the following hypotheses:

H_0 : The mean distance between the probes in T-ALL is greater than or equal to the distance between the probes in T-cells or the mean distance between the probes in treated T-ALL is greater than or equal to the distance between the probes in untreated T-ALL.

$$\text{Example : } \mu_{\text{T-ALL}} \geq \mu_{\text{T cells}}$$

H_A : The mean distance between the probes in T-ALL is smaller than the distance between the probes in T-cells or the mean distance between the probes in treated T-ALL is smaller than the distance between the probes in untreated T-ALL.

$$\text{Example : } \mu_{\text{T-ALL}} < \mu_{\text{T cells}}$$

The number (*n*) of independent replicates tested and the statistical test used in each case are described in the respective figure legends; exact *P* values are indicated in the respective figure in all cases.

Reporting Summary. Further information on research design is available in the Nature Research Reporting Summary linked to this article.

Data availability

All sequencing data created in this study have been uploaded to the Gene Expression Omnibus (GEO; <https://www.ncbi.nlm.nih.gov/geo/>) and are available

under accession code [GSE115896](#). Biological material used in this study can be obtained from the authors upon request. Source data for Figs. 2–6 and Extended Data Figs. 1–3, 5, 7, 9 and 10 are provided with the paper.

Code availability

All code for Hi-C analysis is available within the previously published Hi-C bench platform (<https://github.com/NYU-BFX>).

References

63. Pitt, L. A. et al. CXCL12-producing vascular endothelial niches control acute T cell leukemia maintenance. *Cancer Cell* **27**, 755–768 (2015).
64. Rao, S. S. P. et al. A 3D map of the human genome at kilobase resolution reveals principles of chromatin looping. *Cell* **159**, 1665–1680 (2014).
65. Strikoudis, A. et al. Regulation of transcriptional elongation in pluripotency and cell differentiation by the PHD-finger protein Phf5a. *Nat. Cell Biol.* **18**, 1127–1138 (2016).
66. Phanstiel, D. H., Boyle, A. P., Heidari, N. & Snyder, M. P. Mango: a bias-correcting ChIA-PET analysis pipeline. *Bioinformatics* **31**, 3092–3098 (2015).

Acknowledgements

We thank all members of the Aifantis and Tsirigos laboratories for discussions throughout this project; A. Heguy and the NYU Genome Technology Center (supported in part by National Institutes of Health (NIH)/National Cancer Institute (NCI) grant P30CA016087-30) for expertise with sequencing experiments; the NYU Flow Cytometry facility for expert cell sorting; the Applied Bioinformatics Laboratory for computational assistance; and Genewiz for expertise with sequencing experiments. This work has used computing resources at the High-Performance Computing Facility at the NYU Medical Center. We would also like to acknowledge B. Ren and A. Schmitt for their support on the Hi-C experiments. I.A. is supported by the NCI/NIH (1P01CA229086, 1R01CA228135, R01CA216421, R01CA202025, R01CA133379, R01CA149655 and 1R01CA194923), Alex's Lemonade Stand Cancer Research Foundation, the Chemotherapy Foundation, the Leukemia and Lymphoma Society and the NYSTEM program of the New York State Health Department. A.T. is supported by the American Cancer Society (RSG-15-189-01-RMC), the NCI/NIH (1P01CA229086), the Leukemia and Lymphoma Society and St. Baldrick's Foundation. P.T. was previously supported by an AACR Incyte Corporation Leukemia Research Fellowship and is currently supported by a Young Investigator Grant from Alex's Lemonade Stand Cancer Research Foundation. P.N. was supported by the NCI (R00CA188293), the American Society of Hematology, the Zell Foundation, the H Foundation and a grant (U54CA193419) from the NCI and the Chicago Region Physical Sciences–Oncology Center (CR-PSOC). P.V.V. was supported by a European Research Council Starting Grant (639784). T.L. is supported by the National Institute of General Medical Sciences (NIGMS)/NIH (R01GM127538). F.B. is supported by a Young Investigator Grant from Alex's Lemonade Stand Cancer Research Foundation. S.N. is supported by the Onassis Foundation (scholarship ID F ZP 036-1/2019-2020).

and Lymphoma Society and St. Baldrick's Foundation. P.T. was previously supported by an AACR Incyte Corporation Leukemia Research Fellowship and is currently supported by a Young Investigator Grant from Alex's Lemonade Stand Cancer Research Foundation. P.N. was supported by the NCI (R00CA188293), the American Society of Hematology, the Zell Foundation, the H Foundation and a grant (U54CA193419) from the NCI and the Chicago Region Physical Sciences–Oncology Center (CR-PSOC). P.V.V. was supported by a European Research Council Starting Grant (639784). T.L. is supported by the National Institute of General Medical Sciences (NIGMS)/NIH (R01GM127538). F.B. is supported by a Young Investigator Grant from Alex's Lemonade Stand Cancer Research Foundation. S.N. is supported by the Onassis Foundation (scholarship ID F ZP 036-1/2019-2020).

Author contributions

A.T. and I.A. conceived, designed and supervised the study with input from A.K., P.T. and P.N. A.K. designed and performed most of the computational analyses with help from A.T., S.N. and C.L. P.T. and P.N. designed and performed most of the experiments with help from Y.G., X.C., H.H., S.B., J.W., T.T., Y.F., F.B., Y.Z., E.P., P.V.V., G.G.I. and T.L. P.T., P.N. and Y.G. performed Hi-C, HiChIP and 4C experiments with help from X.C., S.B., J.W. and Y.Z. P.T. performed DNA FISH with help from Y.F. and T.L. P.T. performed ChIP-seq with help from P.N., S.B. and J.W. P.T. and H.H. performed RNA-seq. T.T. performed GRO-seq. A.T., I.A., A.K. and P.T. wrote the manuscript with input from all authors.

Competing interests

A.T. is a scientific advisor to Intelligencia.AI. All other authors declare that they have no competing interests.

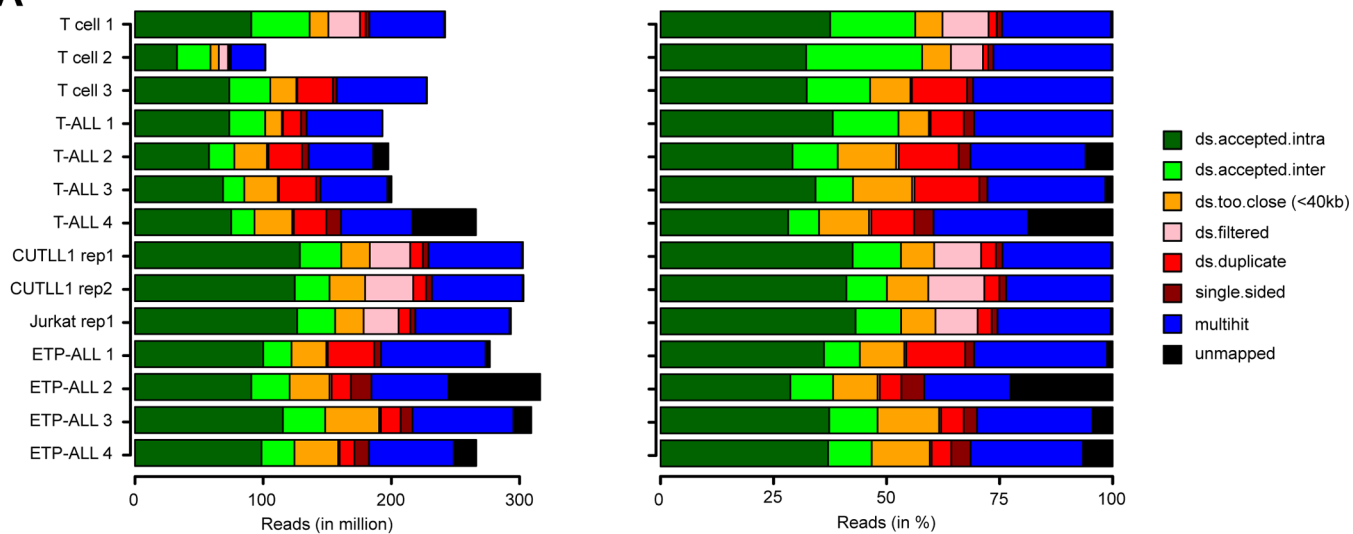
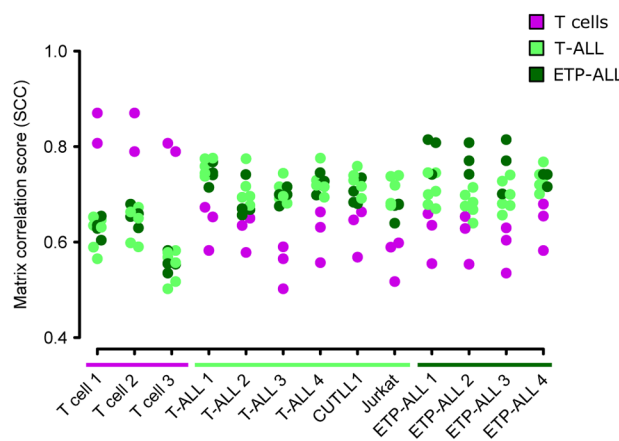
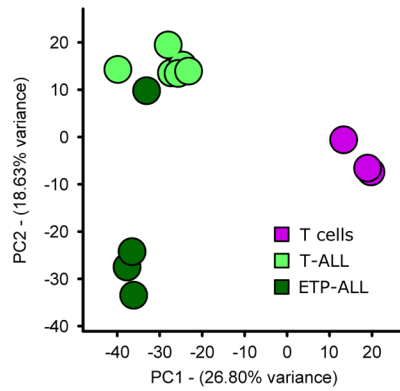
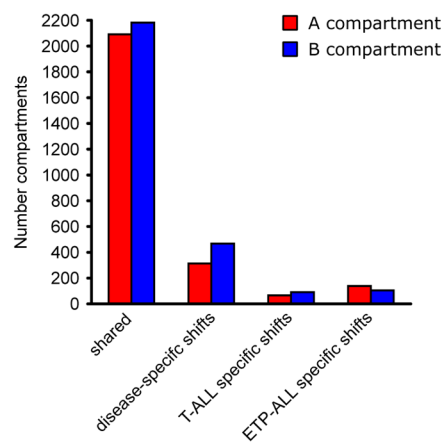
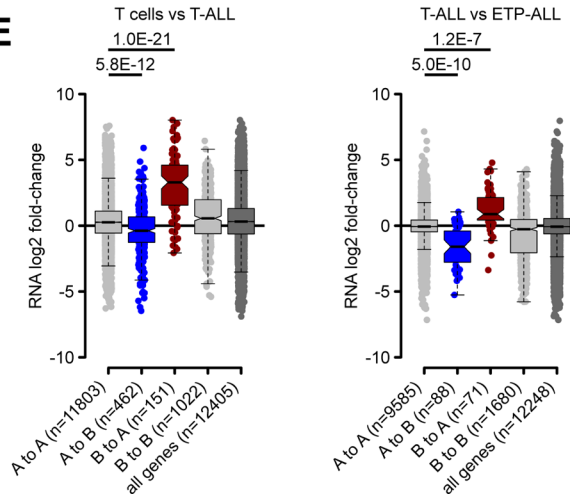
Additional information

Extended data is available for this paper at <https://doi.org/10.1038/s41588-020-0602-9>.

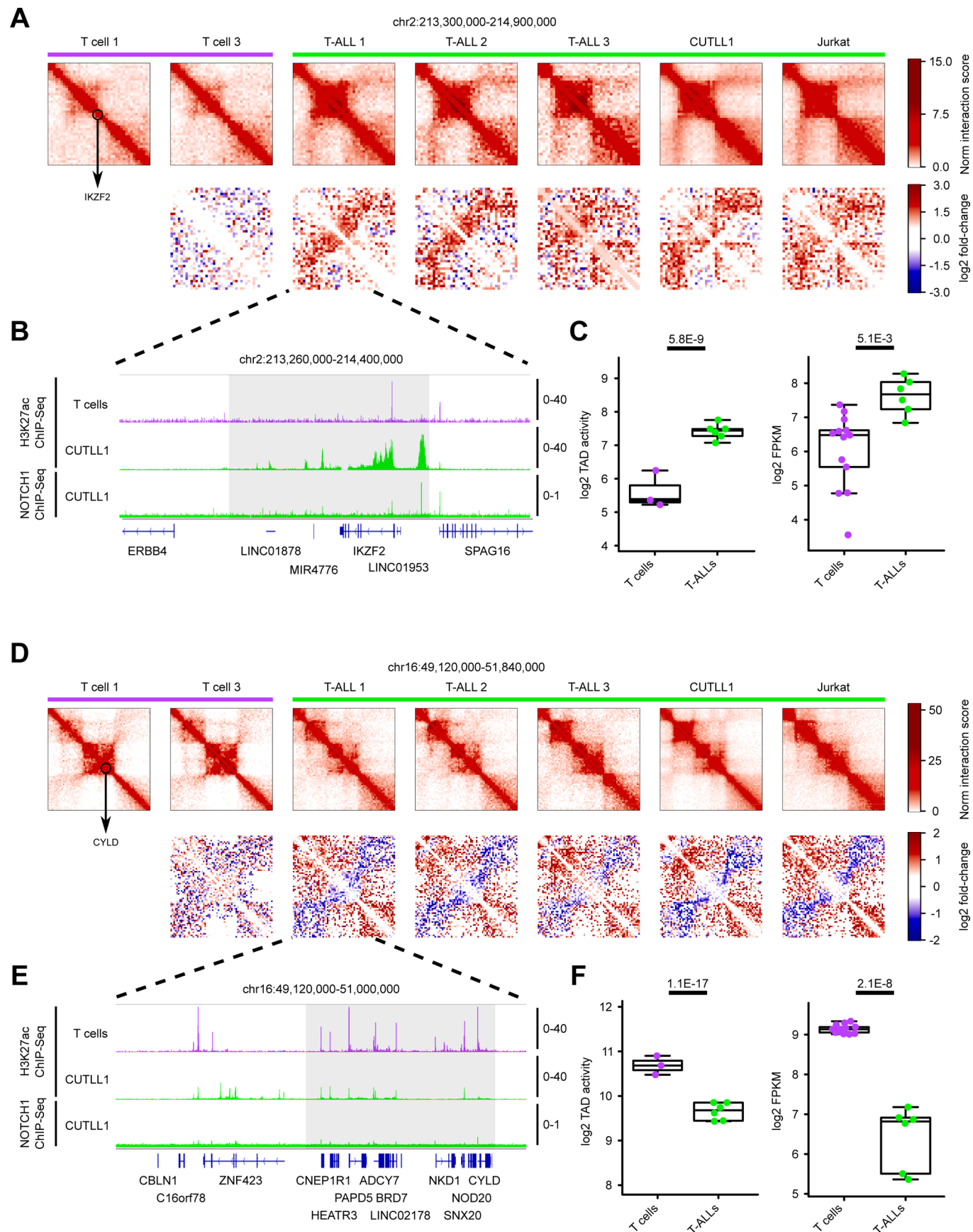
Supplementary information is available for this paper at <https://doi.org/10.1038/s41588-020-0602-9>.

Correspondence and requests for materials should be addressed to I.A. or A.T.

Reprints and permissions information is available at www.nature.com/reprints.

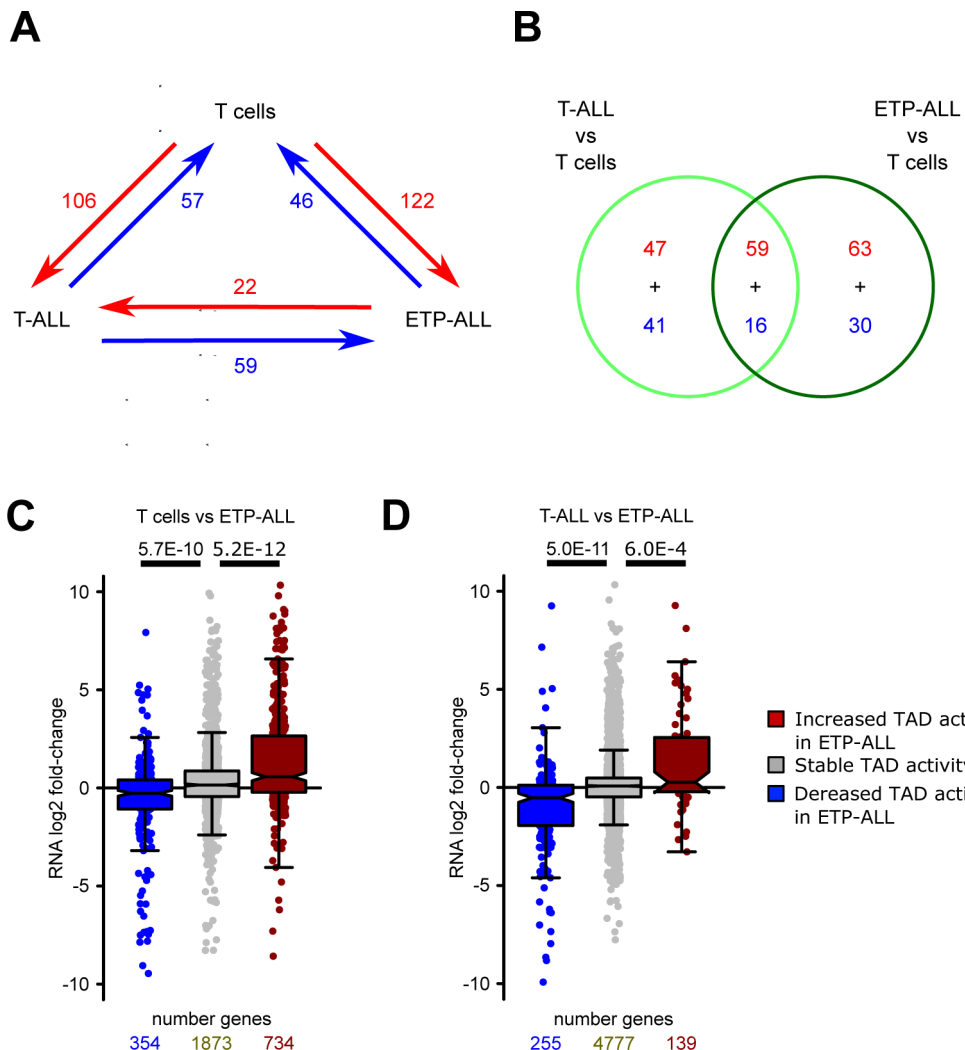
A**B****C****D****E****Extended Data Fig. 1 | See next page for caption.**

Extended Data Fig. 1 | Hi-C quality control and unsupervised analyses. **a)** Read alignment statistics for Hi-C datasets, as absolute reads (left) and relative reads (in %, right). “ds.accepted.intra” are all intra-chromosomal reads used for all downstream analyses. **b)** Genome-wide stratum-adjusted correlation coefficient (SCC) scores for all pair-wise comparisons of the Hi-C datasets. HiCRep was used to calculate chromosome-wide correlation scores, which were averaged across all chromosomes for each pair-wise comparison. The HiCRep smoothing parameter X was set to 1.0. **c)** Principal Component Analysis (PCA) of the genome-wide compartment scores for each Hi-C dataset. Number samples: T cells n=3; T-ALL n=6, ETP-ALL n=4. **d)** Compartment shifts between T cells, T-ALL and ETP-ALL. Assignment of A compartment was done using an average c-score > 0.1 in either all T cell, T-ALL or ETP-ALL samples and B compartment with average c-score < -0.1. Significance for differences between pairwise comparisons of T cells, T-ALL and ETP-ALL was determined using a two-sided *t* test between c-scores, and compartment shifts were determined using P value < 0.1. **e)** Integration of gene expression associated with compartment shifts for comparisons of T cell vs T-ALL (left) or T-ALL vs ETP-ALL (right) using RNA-seq (FPKM > 1). For each gene within the respective compartment bin, log₂ fold-change between T cells and T-ALL (left) or between T-ALL and ETP-ALL (right) is shown. Significant differences are calculated using an unpaired one-sided *t* test comparing genes from A to A compartments (that is active compartment) with genes from A to B or B to A compartment shifts, following the hypothesis of a positive correlation between expression and compartment association. Boxplot information can be found as additional Source Data.

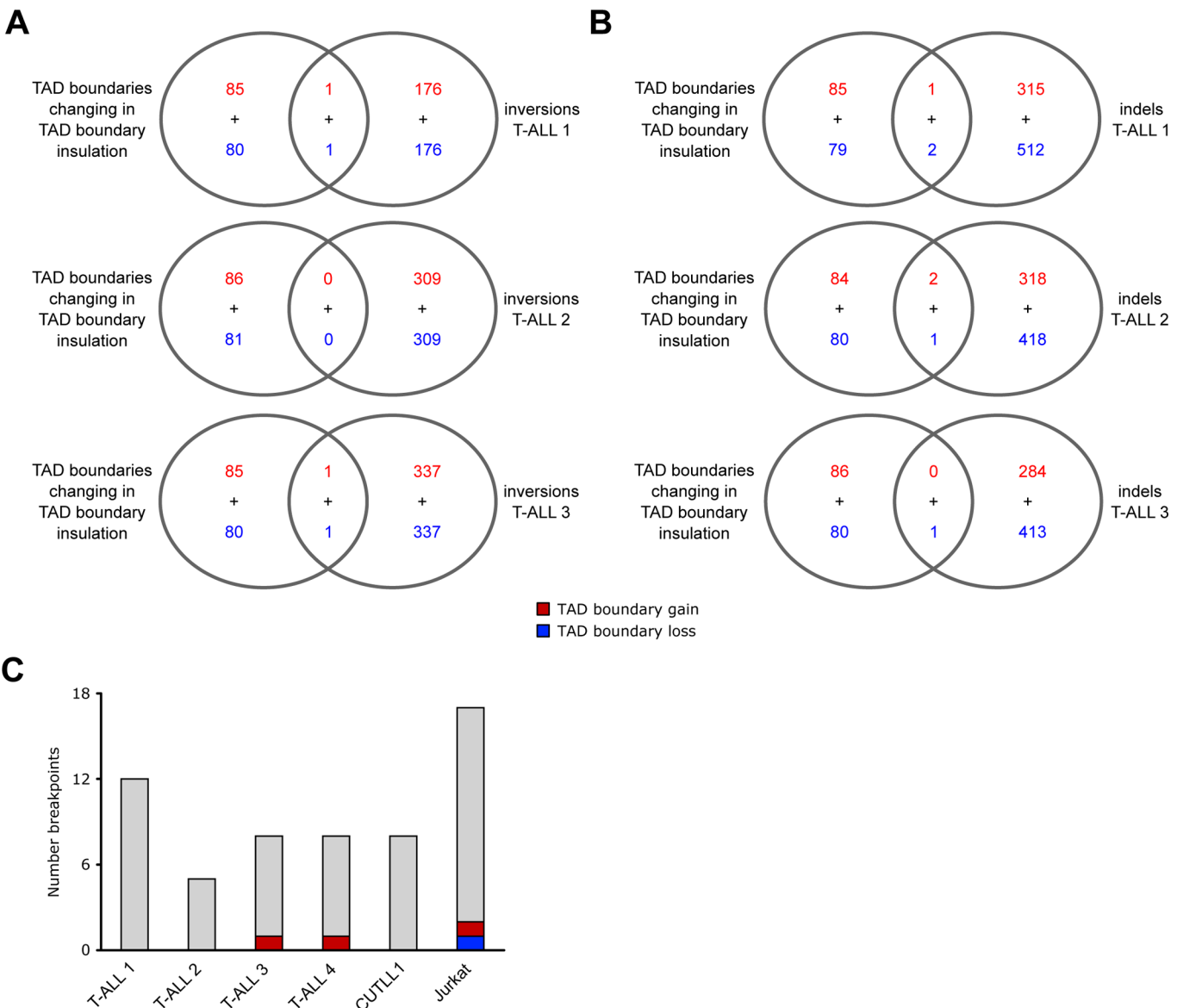


Extended Data Fig. 2 | See next page for caption.

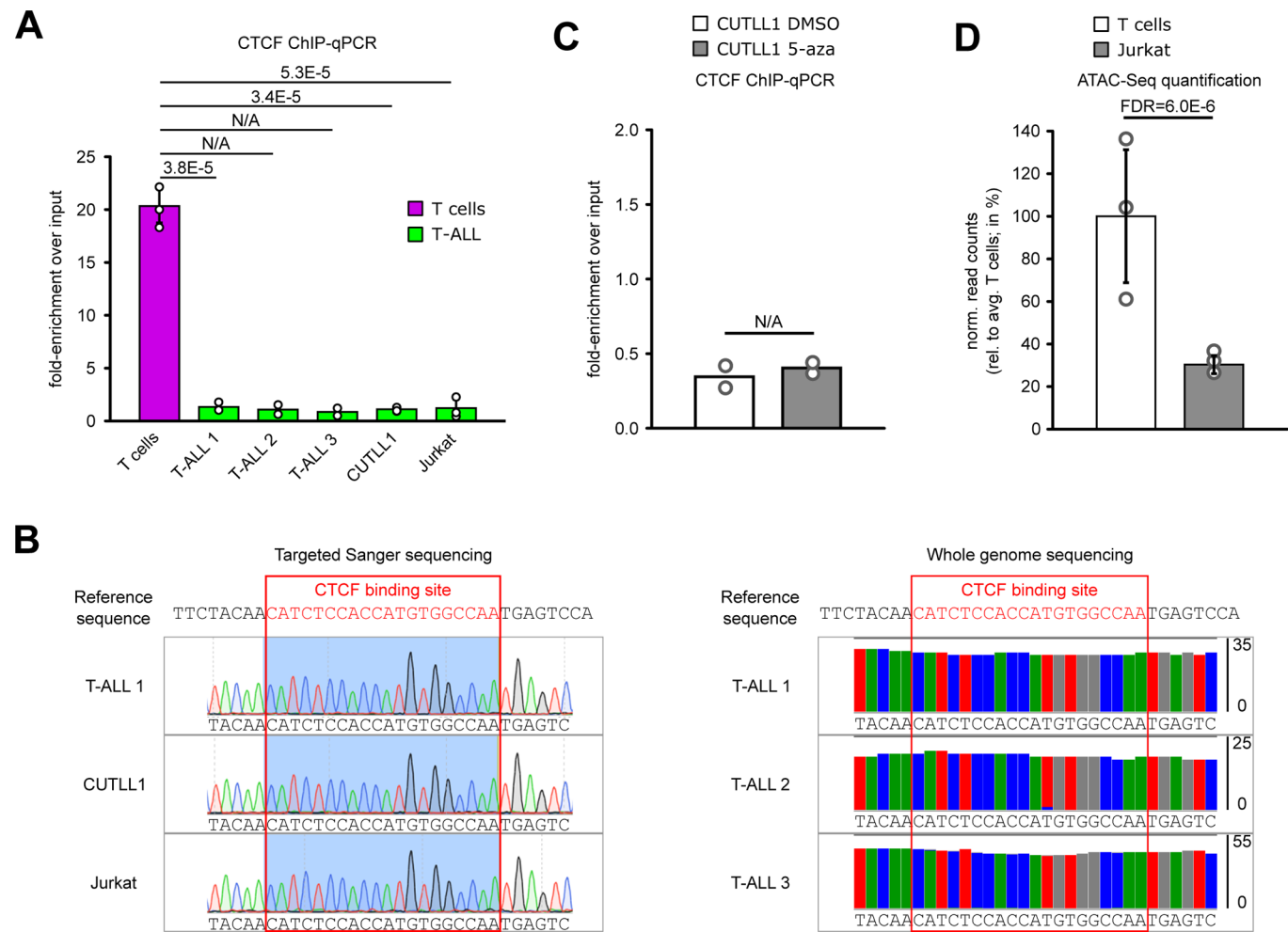
Extended Data Fig. 2 | Genomic loci displaying differential intra-TAD activity in T-ALL. **a**) Hi-C interaction heat maps (first row) showing the *IKZF2* locus (black circle). Second row shows heat maps of log2 (fold-change) interactions compared to T cell 1. **b**) H3K27ac ChIP-seq tracks for *IKZF2* locus in T cells and CUTLL1, NOTCH1 ChIP-seq tracks for CUTLL1. Tracks represent fold-enrichment over input where applicable and counts-per-million reads otherwise. Grey area indicates TAD containing *IKZF2*. Number replicates: T cells H3K27ac n=2; CUTLL1 H3K27ac n=2; CUTLL1 NOTCH1 n=1. **c**) Quantifications for intra-TAD activity (left; as highlighted in **a**) and expression of *IKZF2* (right). Statistical evaluation for intra-TAD activity was performed using paired two-sided *t* test of average per interaction-bin for *IKZF2* TAD between T cells (n=3) and T-ALL (n=6), followed by multiple testing correction. Log2 FPKM of *IKZF2* expression for T cells (n=13) and T-ALL (n=6) samples; statistical evaluation was performed using edgeR followed by multiple testing correction. **d**) Hi-C interaction heat maps (first row) showing the *CYLD* locus (black circle). Second row shows heat maps of log2 (fold-change) interactions when compared to T-cell 1. **e**) H3K27ac ChIP-seq tracks for *CYLD* locus in T cells and CUTLL1, NOTCH1 ChIP-seq tracks for CUTLL1. Tracks represent fold-enrichment over input where applicable and counts-per-million reads otherwise. Grey area indicates TAD containing *CYLD*. Number replicates: T cells H3K27ac n=2; CUTLL1 H3K27ac n=2; CUTLL1 NOTCH1 n=1. **f**) Quantifications for intra-TAD activity (left; as highlighted in **D**) and expression of *CYLD* (right). Statistical evaluation for intra-TAD activity was performed using paired two-sided *t* test of average per interaction-bin for *CYLD* TAD between T cells (n=3) and T-ALL (n=6), followed by multiple testing correction (see methods). Log2 FPKM of *CYLD* expression for T cells (n=13) and T-ALL (n=6); statistical evaluation was performed using edgeR followed by multiple testing correction. Boxplot information can be found as additional Source Data.



Extended Data Fig. 3 | Intra-TAD activity cross-comparison of T-ALL sub-types. **a)** Comparisons of intra-TAD activity between T cells, T-ALL and ETP-ALL samples. **b)** Overlap of differentially active TADs between the two comparisons of T cells vs T-ALL and T cells vs ETP-ALL, visualized as venn diagram. Red and blue colors correspond to differences as highlighted in **a**. **c, d)** Integration of RNA-seq (FPKM > 1) within TADs with decreased / increased intra-TAD activity for ETP-ALL vs T cells (**c**) and ETP-ALL vs T-ALL (**d**). For each such gene, the log₂ (fold-change) in expression between ETP-ALL and T cells (**c**) / T-ALL and ETP-ALL (**d**) taken from RNA-seq is shown. Significant differences are calculated by an unpaired one-sided *t* test comparing genes from TADs with decreased / increased intra-TAD activity with genes from stable TADs, following the hypothesis of a positive correlation between expression and intra-TAD activity changes. Boxplot information can be found as additional Source Data.

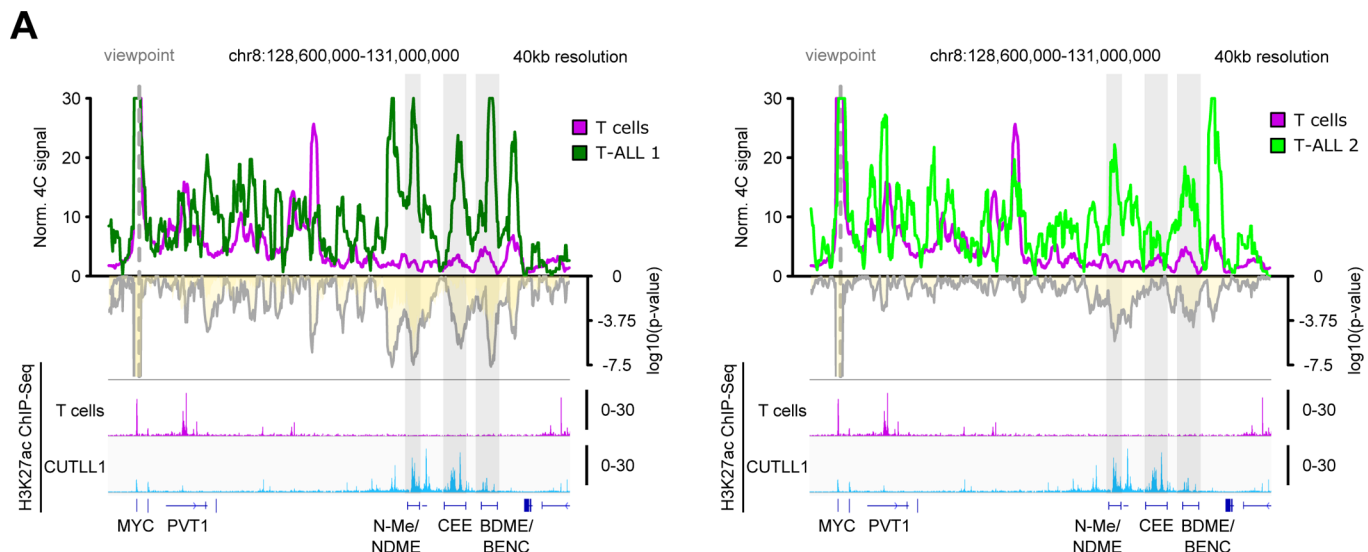


Extended Data Fig. 4 | WGS integration with TAD boundaries altered in T-ALL. **a, b)** Overlap of altered TAD boundaries as in Fig. 3c, d with genomic inversions (**a**) or insertions/deletions (indels) (**b**) from WGS of T-ALL 1 (top) and T-ALL 2 (bottom). Overlap was determined by bedtools intersect, using a 1bp overlap for indels and 100 kb for individual inversion breakpoints (instead of the entire genomic range affected by the inversion). **c)** Overlap of individual translocation breakpoints (calculated from T-ALL Hi-C samples as in Supplementary Fig. 1B) with TAD boundaries displaying changes in TAD insulation between T cells and T-ALL. Overlap was determined by bedtools intersect, using a 1bp overlap.

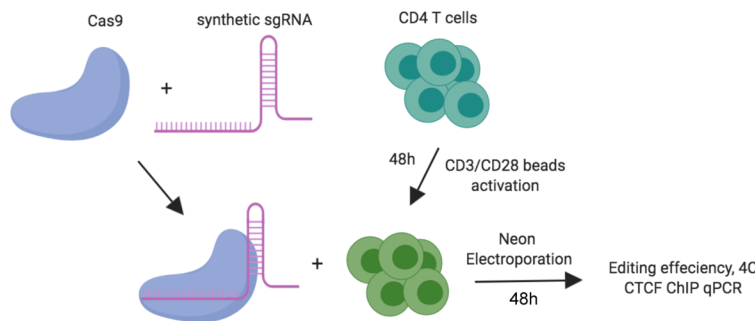


Extended Data Fig. 5 | Difference in CTCF insulation in MYC locus is not due to genomic mutation but potentially regulated by open chromatin.

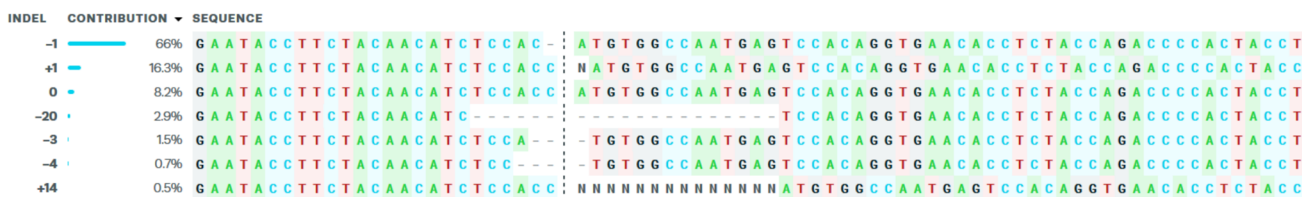
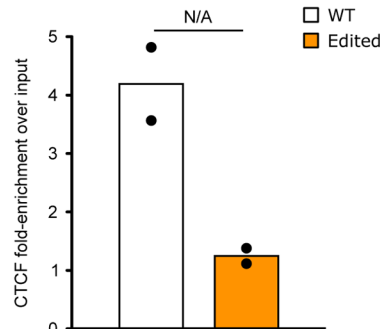
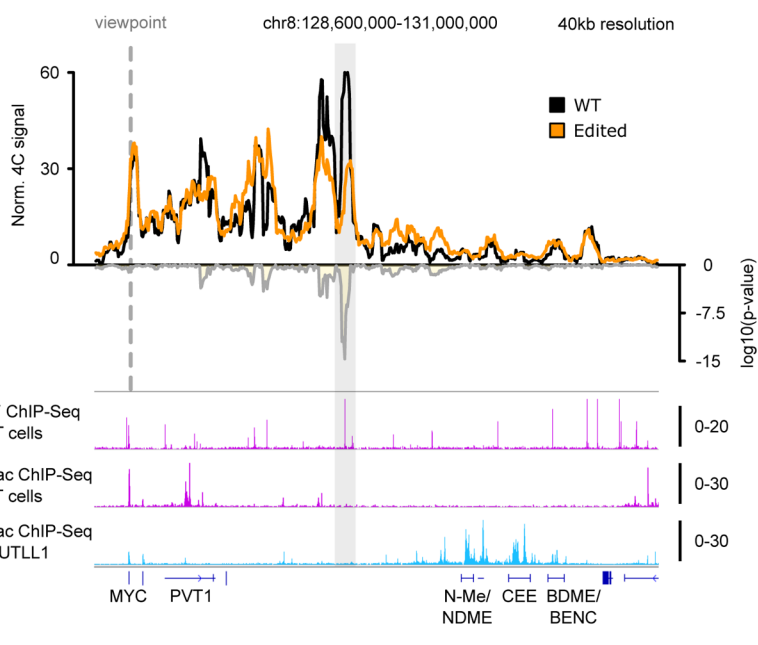
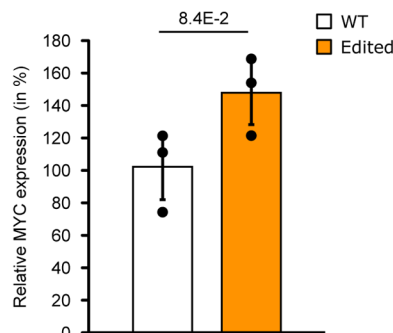
a) CTCF ChIP-qPCR of the CTCF binding site in the lost MYC TAD boundary, shown as fold-enrichment over input. Significant differences compared to T cells were calculated with an unpaired one-sided t test, following the hypothesis of loss of CTCF binding in T-ALL samples as determined from the genome-wide analysis ($n=3$ replicates for T cells, T-ALL 1, T-ALL 2, CUTLL1 and Jurkat; $n=2$ replicates for T-ALL 3 and T-ALL 4). Error bars indicate s.d.; center value indicates mean. **b**) Targeted sanger sequencing indicates no mutation in T-ALL in the CTCF binding site at the MYC TAD boundary. Tracks show chromatogram of individual base calls (left). Whole genome sequencing indicates no mutation in T-ALL in the motif of CTCF binding site. Tracks show (mis-)matches compared to reference sequence in all reads covering the respective genomic position (right). **c**) CTCF ChIP-qPCR before and after treatment with global DNA-demethylating agent 5-azacytidine ($n=2$ replicates). **d**) ATAC-seq quantification for T cells and Jurkat for the genomic area covering loss of CTCF binding in the downstream TAD boundary of MYC. Data was normalized to the average T cell signal, shown in percent ($n=3$ replicates). Statistical evaluation was performed using DiffBind with edgeR-method, following multiple testing correction. Error bars indicate s.d.; center value indicates mean.



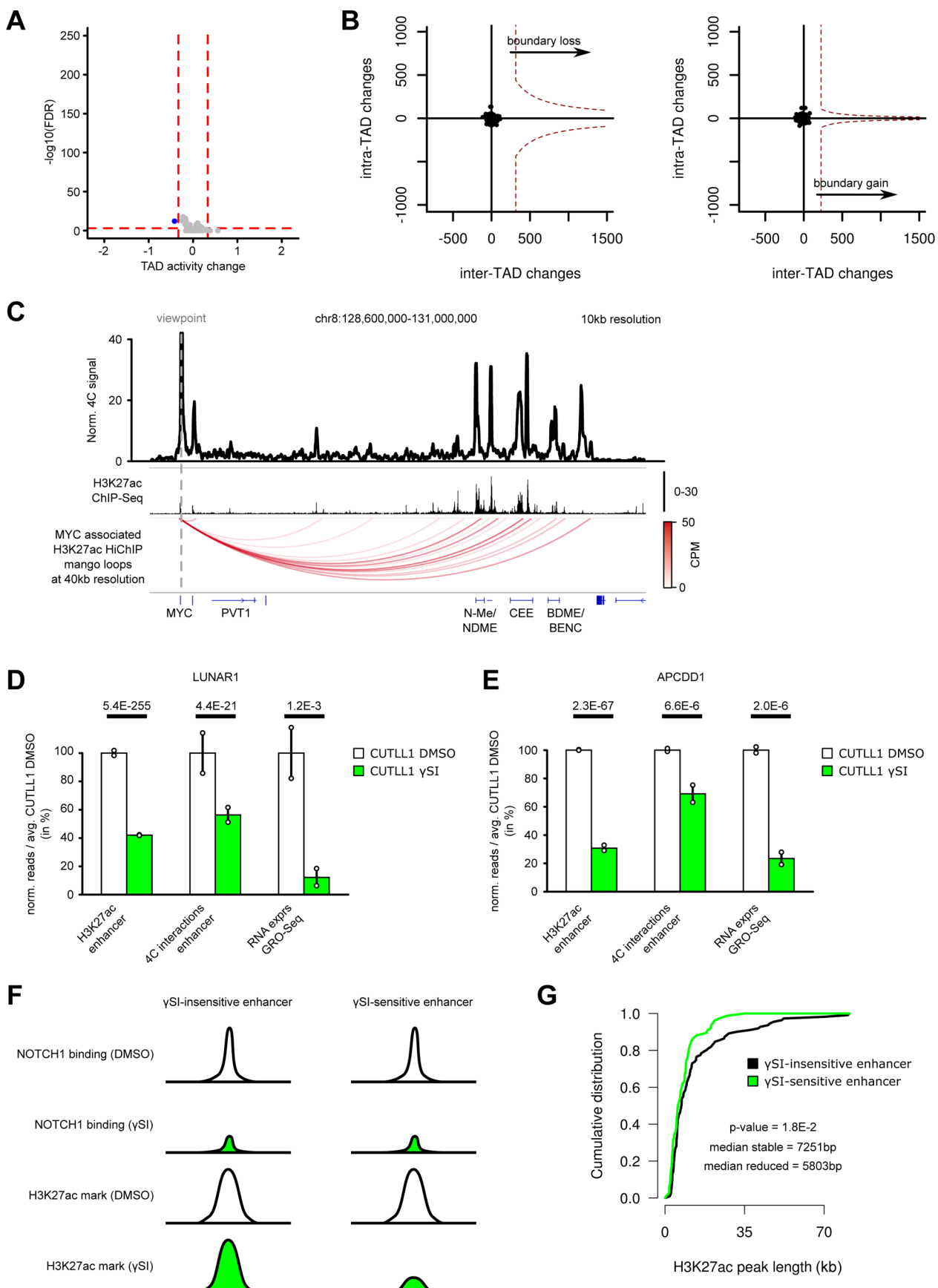
Extended Data Fig. 6 | 4C-Seq validation of MYC super-enhancer interaction in primary T-ALL. **a)** 4C-seq analysis using MYC promoter as viewpoint. Positive y-axis shows interactions with the MYC promoter viewpoint as normalized read counts, negative y-axis shows significance of differential interactions between T cells and primary T-ALL samples as $\log_{10}(P \text{ value})$ derived using edgeR function glmQLFTest. H3K27ac ChIP-seq tracks for T cells and CUTLL1 are represented below as fold-enrichment over input. Grey areas indicate MYC super-enhancer elements. Number replicates: T cells 4 C n=2; T-ALL 1 4 C n=1; T-ALL 2 4 C n=2; T cells H3K27ac n=2; CUTLL1 H3K27ac n=2.

A**B**

CTCF binding site
GAATAACCTTCTACAACATCTCCACCATGTGGCCAATGAGTCCACAGGTGAACACCTTACCAAGACCCACTACCT
guide RNA

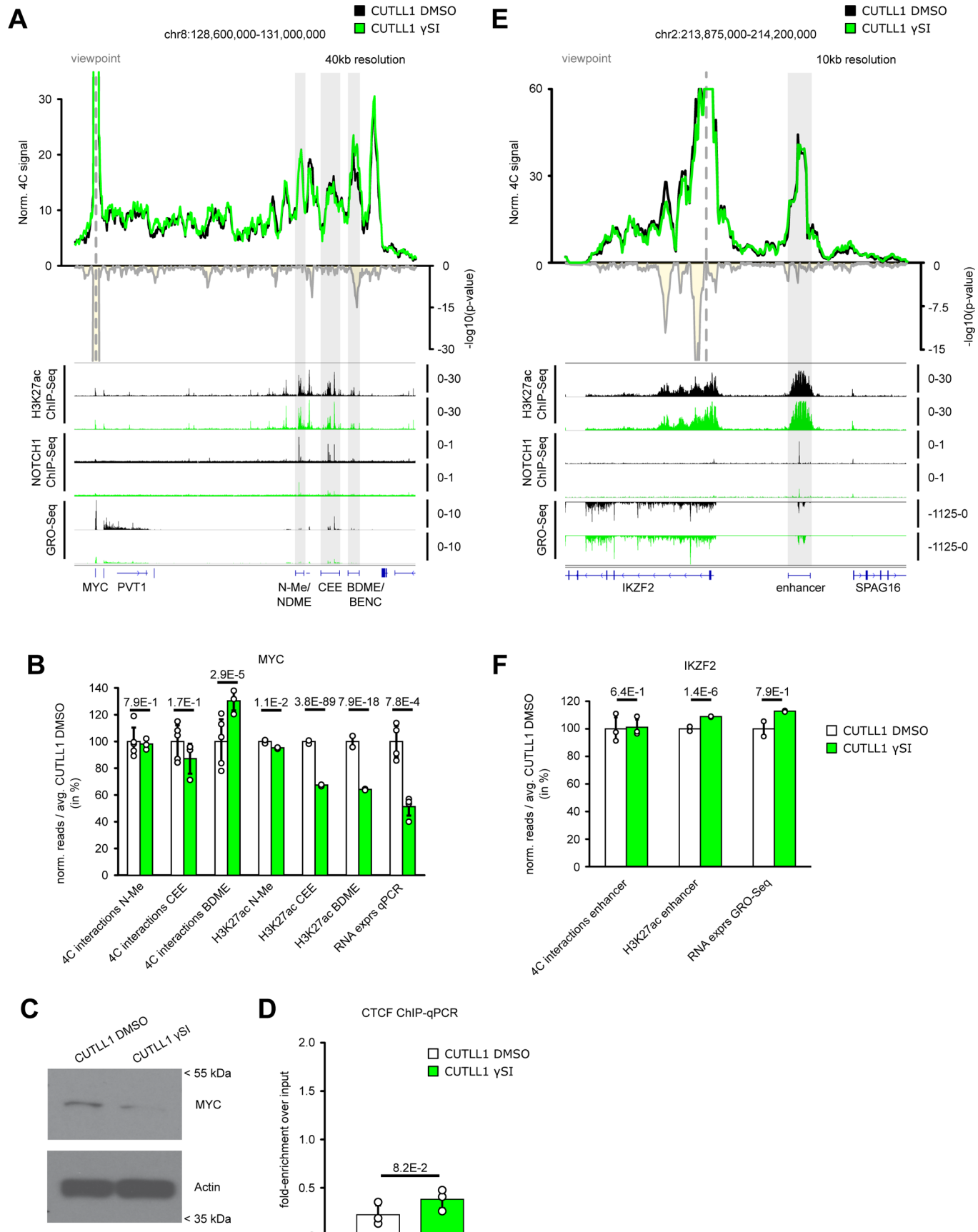
**C****E****D**

Extended Data Fig. 7 | CRISPR-Cas9 deletion of CTCF binding site shows loss of insulation around MYC locus. **a)** Schematic of Cas9+Synthetic guide transfection of activated T cells. **b)** Sequence showing CTCF motif in the insulator region in T cells targeted for CRISPR-based deletion. sgRNA targeting sequence within the CTCF motif is highlighted. Sequencing of sgRNA target site indicates various indels along with frequencies observed for each indel. **c)** CTCF ChIP-qPCR validation of reduced CTCF binding in edited T cells compared to unedited T cells ($n=2$ replicates). **d)** qPCR comparing MYC expression in edited T cells compared to unedited T cells ($n=3$ replicates). Statistical significance was determined using unpaired two-sided *t* test. Error bars indicate s.d.; center value indicates mean. **e)** 4C-seq analysis using MYC promoter as viewpoint in edited and unedited T cells. Positive y-axis shows interactions with the viewpoint as normalized read counts, negative y-axis shows significance of differential interactions between the two samples as log₁₀(P value) calculated with edgeR function glmQLFTest. Tracks below show CTCF ChIP-seq in CUTLL1 and H3K27ac ChIP-seq in naïve T cells and CUTLL1 as fold-enrichment over input. Grey area indicates deleted CTCF binding site. Number replicates: T cells WT 4C $n=2$; T cells Edited 4C $n=2$; T cells CTCF $n=2$; T cells H3K27ac $n=2$; CUTLL1 H3K27ac $n=2$.



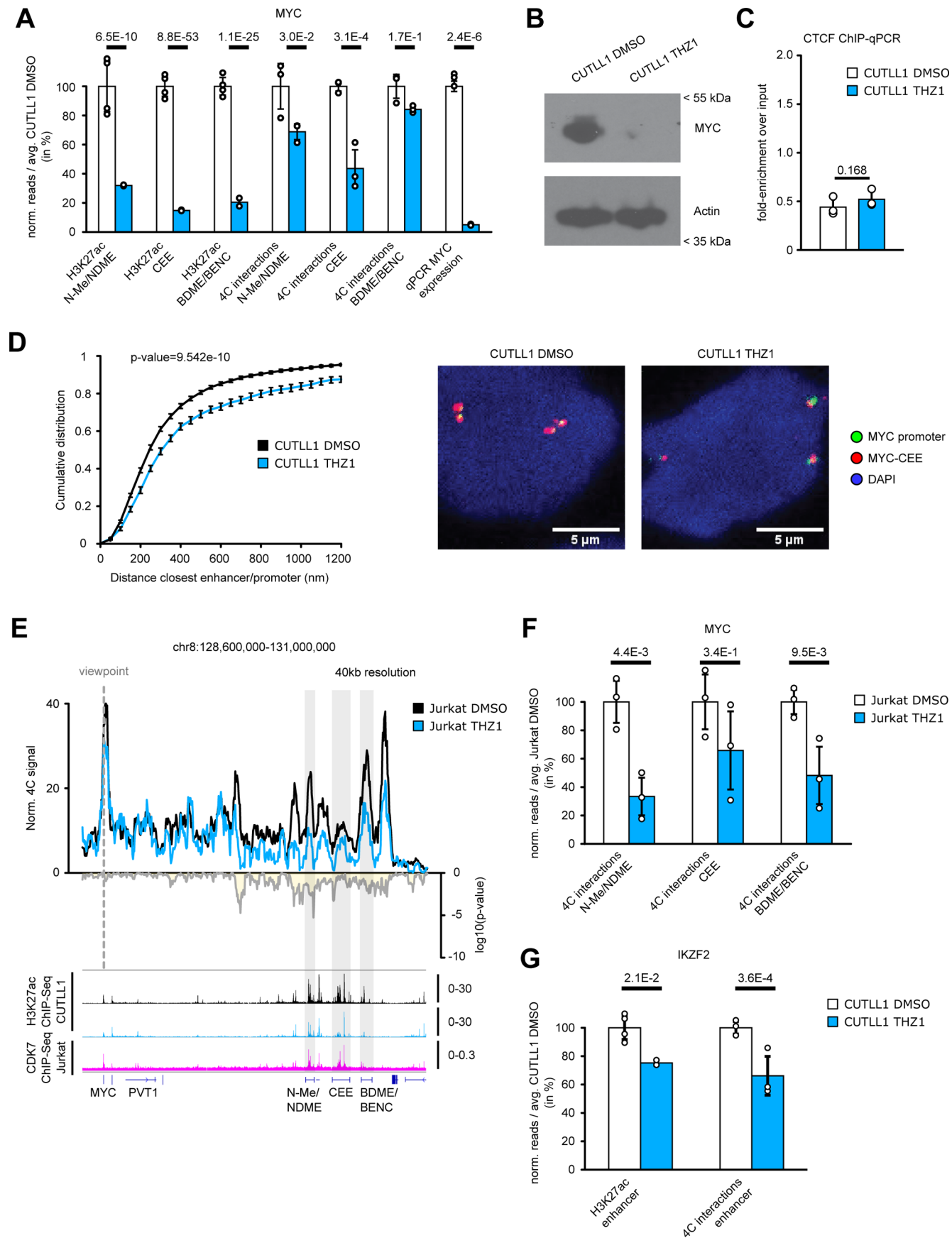
Extended Data Fig. 8 | See next page for caption.

Extended Data Fig. 8 | Genome-wide Hi-C analysis in T-ALL following γ SI shows no intra-TAD activity differences, but individual promoter-enhancer loops are disrupted. **a)** Volcano plot showing differential intra-TAD activity between CUTLL1 DMSO vs CUTLL1 γ SI (average activity $> 0.58 / < -0.58$ and with FDR < 0.05). Statistical evaluation was performed using paired two-sided *t* test between all per bin-interactions between DMSO and γ SI ($n=2$ replicates). **b)** Representation of TAD boundary alteration events (red dots; none identified). Plots depict pair-wise comparisons for TAD boundary losses of adjacent CUTLL1 (untreated, left) TADs and for TAD boundary gains of adjacent CUTLL1 (γ SI treated, right) TADs. Dotted line represents outlier threshold as in Fig. 3**c**) and **d**). **c)** Virtual 4C of H3K27ac ChIP in CUTLL1, using MYC promoter as viewpoint (chr8: 128,747,680), showing edgeR-normalized CPM. H3K27ac ChIP-seq track for MYC locus shown as fold-enrichment over input. Detected significant loops as arc-representation (below) from mango pipeline utilizing two-sided binomial test per matrix-diagonal followed by multiple testing correction⁶⁶ (FDR < 0.1 ; CPM > 5). Number replicates: CUTLL1 H3K27ac ChIP n=1; CUTLL1 H3K27ac ChIP-seq n=2. **d)** H3K27ac signal (enrichment over input) (left), chromatin interaction of the highest peak by 4C-seq (center) for the interaction of *LUNAR1* promoter with its upstream enhancer and *LUNAR1* expression (right). All quantifications are normalized to the respective average T cell signal, shown in percent. Significance of differences was calculated using diffBind with edgeR-method (for H3K27ac ChIP-seq, FDR) and edgeR (for 4C-seq interactions and GRO-seq as P value and FDR respectively). Error bars indicate s.d.; center value indicates mean. Number replicates: CUTLL1 DMSO H3K27ac n=2; CUTLL1 γ SI H3K27ac n=2; CUTLL1 DMSO 4C n=2; CUTLL1 γ SI 4C n=2; CUTLL1 DMSO GRO-seq n=2; CUTLL1 γ SI GRO-seq n=2. **e)** H3K27ac signal (left), chromatin interaction of the highest peak by 4C-seq (center) for the interaction of *APCDD1* enhancer with the downstream *APCDD1* promoter and *APCDD1* expression (right). All quantifications are normalized to the respective average T cell signal, shown in percent. Significance of differences was calculated using diffBind with edgeR-method (for H3K27ac ChIP-seq, FDR) and edgeR (for 4C-seq interactions and GRO-seq as P value and FDR respectively). Error bars indicate s.d.; center value indicates mean. Number replicates: CUTLL1 DMSO H3K27ac n=2; CUTLL1 γ SI H3K27ac n=2; CUTLL1 DMSO 4C n=2; CUTLL1 γ SI 4C n=2; CUTLL1 DMSO GRO-seq n=2; CUTLL1 γ SI GRO-seq n=2. **f)** Schematic of γ SI sensitive and insensitive enhancer. **g)** Peak width of stable (black; $n=111$) or decreased H3K27ac signal (green, $n=76$) as defined in Fig. 5a. Significant difference between the distributions is estimated by a two-sided Wilcoxon test. Number replicates: CUTLL1 DMSO H3K27ac n=2; CUTLL1 γ SI H3K27ac n=2.



Extended Data Fig. 9 | See next page for caption.

Extended Data Fig. 9 | Treatment with γ SI does not alter all NOTCH1 dynamic enhancers. **a)** 4C-seq using MYC promoter as viewpoint. Positive y-axis shows interactions with viewpoint as normalized read counts, negative y-axis shows significance of differential interactions as log₁₀(P value) calculated using edgeR function glmQLFTest (CUTLL1 DMSO n=5; CUTLL1 γ SI n=3). Tracks below show H3K27ac, NOTCH1 ChIP-seq and GRO-seq (positive strand only) as fold-enrichment where applicable, and counts-per-million reads otherwise. Grey areas indicate MYC super-enhancer elements. **b)** Quantification of H3K27ac signal (enrichment over input), chromatin interactions by 4C-seq for the interactions of MYC promoter and MYC expression. Interaction changes are measured by centering the 40 kb bin on highest peaks within N-Me/NDME, CEE or BDME/BENC elements. MYC expression was measured by qPCR. All quantifications are normalized to CUTLL1 DMSO, shown in percent. Error bars indicate s.d.; center value indicates mean. Significance is shown as false-discovery rate (FDR) for H3K27ac signal change (R package DiffBind with edgeR-method), P value for chromatin interaction change (edgeR function glmQLFTest) or one-tailored t test for qPCR changes. **c)** Cropped western blot images immunoblotted with MYC antibody. Unprocessed western blots can be found as Source Data. Experiment was repeated twice with similar results. **d)** CTCF ChIP-qPCR of lost MYC boundary upon γ SI in CUTLL1 (n=3). Error bars indicate s.d.; center value indicates mean. Significance was calculated using unpaired two-sided t test. **e)** 4C-seq analysis using IKZF2 promoter as viewpoint after γ SI treatment. Positive y-axis shows normalized read counts, negative y-axis shows significance of differential interactions as log₁₀(P value) calculated using edgeR function glmQLFTest (CUTLL1 DMSO n=3; CUTLL1 γ SI n=3). Tracks below show H3K27ac, NOTCH1 ChIP-seq and GRO-seq (negative strand only) as fold-enrichment over input where applicable, and counts-per-million reads otherwise. Grey area indicates IKZF2 enhancer. **f)** H3K27ac signal is specific for enhancer highlighted in **d)**. Interaction changes are measured by centering the 40 kb bin on the highest enhancer peak. IKZF2 expression after γ SI treatment was measured by GRO-seq. All quantifications are normalized to the average T cell signal, shown in percent. Error bars indicate s.d.; center value indicates mean. Significance is shown as false-discovery rate (FDR) for H3K27ac signal (R package DiffBind with edgeR-method), P value for chromatin interaction (edgeR function glmQLFTest) or one-tailored t test for qPCR expression.



Extended Data Fig. 10 | See next page for caption.

Extended Data Fig. 10 | Treatment of T-ALL with THZ1 reduces also γSI insensitive promoter-enhancer interactions. **a)** H3K27ac signal is specific for N-Me/NDME, CEE and BDME/BENC. Interaction changes are measured by centering the 40 kb bin on highest peaks within N-Me/NDME, CEE or BDME/BENC elements. MYC expression after THZ1 treatment was measured by qPCR. All quantifications are normalized to the average CUTLL1 DMSO signal, shown in percent. Error bars indicate s.d.; center value indicates mean. Significance is shown as false-discovery rate (FDR) for H3K72ac signal (R package DiffBind with edgeR-method), P value for chromatin interaction (edgeR function glmQLFTTest) or two-sided t test for qPCR expression. **b)** Cropped western blot images immunoblotted with MYC antibody. Unprocessed western blots can be found as Source Data. Experiment was repeated twice with similar results. **c)** CTCF ChIP-qPCR, shown as enrichment over input, of CTCF site in lost boundary in MYC locus ($n=3$). Error bars indicate s.d.; center value indicates mean. Significance was calculated using unpaired two-sided t test. **d)** Inter-probe distance between MYC promoter and MYC-CEE measured by DNA-FISH analysis. Statistical difference between distributions of probe distances was calculated using two-sample one-sided Kolmogorov Smirnov test. Error bars indicate s.d.; center value indicates median. Probe-pairs CUTLL1 DMSO = 2001. Probe-pairs CUTLL1 THZ1 = 1308. Median distance CUTLL1 DMSO = 264.28 μm. Median distance CUTLL1 THZ1 = 321.69 μm. **e)** 4C-seq using MYC promoter as viewpoint in Jurkat cells. Positive y-axis shows normalized interaction strength with the viewpoint, negative y-axis shows significance of differential interactions as $\log_{10}(P \text{ value})$ calculated using edgeR function glmQLFTTest ($n=3$). Grey areas indicate MYC super-enhancer elements. **f)** Interaction changes are measured by centering the 40 kb bin on N-Me/NDME, CEE or the BDME/BENC. Error bars indicate s.d.; center value indicates mean. Significance is shown as P value for chromatin interaction changes (edgeR function glmQLFTTest). **g)** Quantification of changes in H3K27ac signal (enrichment over input) and chromatin interactions of IKZF2 enhancer in CUTLL1. All quantifications are normalized to the average CUTLL1 DMSO signal, shown in percent. Error bars indicate s.d.; center value indicates mean. Significance is shown as false-discovery rate (FDR) for H3K72ac signal change (R package DiffBind with edgeR-method), P value for chromatin interaction change (edgeR function glmQLFTTest).

Reporting Summary

Nature Research wishes to improve the reproducibility of the work that we publish. This form provides structure for consistency and transparency in reporting. For further information on Nature Research policies, see [Authors & Referees](#) and the [Editorial Policy Checklist](#).

Statistics

For all statistical analyses, confirm that the following items are present in the figure legend, table legend, main text, or Methods section.

n/a Confirmed

- The exact sample size (n) for each experimental group/condition, given as a discrete number and unit of measurement
- A statement on whether measurements were taken from distinct samples or whether the same sample was measured repeatedly
- The statistical test(s) used AND whether they are one- or two-sided
Only common tests should be described solely by name; describe more complex techniques in the Methods section.
- A description of all covariates tested
- A description of any assumptions or corrections, such as tests of normality and adjustment for multiple comparisons
- A full description of the statistical parameters including central tendency (e.g. means) or other basic estimates (e.g. regression coefficient) AND variation (e.g. standard deviation) or associated estimates of uncertainty (e.g. confidence intervals)
- For null hypothesis testing, the test statistic (e.g. F , t , r) with confidence intervals, effect sizes, degrees of freedom and P value noted
Give P values as exact values whenever suitable.
- For Bayesian analysis, information on the choice of priors and Markov chain Monte Carlo settings
- For hierarchical and complex designs, identification of the appropriate level for tests and full reporting of outcomes
- Estimates of effect sizes (e.g. Cohen's d , Pearson's r), indicating how they were calculated

Our web collection on [statistics for biologists](#) contains articles on many of the points above.

Software and code

Policy information about [availability of computer code](#)

Data collection

All NCBI GEO datasets listed in Supplementary Table 2 were downloaded using sra toolkit version 2.8.0.
RNA-Seq data from Chen et al. (see Supplementary Table 2) was downloaded via FTP from data owner upon request.

Data analysis

bowtie2 version 2.3.1. Hi-C bench. genomic-tools. R version 3.3.0. ICE-normalization according to Imakeav et al.. TAD calling by hic-ratio. MACS2 version 2.0.1. bedtools version 2.27.1. diffBind version 2.2.12. IGV version 2.3.83. PWMScan. deeptools version 2.3.3. STAR-aligner version 2.5.0c. ngsutils version 0.5.7. edgeR version 3.14.0. bowtie version 1.0.0. ROSE version 2015. picard-tools version XX. HiCnv.

For manuscripts utilizing custom algorithms or software that are central to the research but not yet described in published literature, software must be made available to editors/reviewers. We strongly encourage code deposition in a community repository (e.g. GitHub). See the Nature Research [guidelines for submitting code & software](#) for further information.

Data

Policy information about [availability of data](#)

All manuscripts must include a [data availability statement](#). This statement should provide the following information, where applicable:

- Accession codes, unique identifiers, or web links for publicly available datasets
- A list of figures that have associated raw data
- A description of any restrictions on data availability

All sequencing data created within this study was uploaded to NCBI GEO (<https://www.ncbi.nlm.nih.gov/geo/>) and is available under the accession GSE115896.

Field-specific reporting

Please select the one below that is the best fit for your research. If you are not sure, read the appropriate sections before making your selection.

- Life sciences Behavioural & social sciences Ecological, evolutionary & environmental sciences

For a reference copy of the document with all sections, see nature.com/documents/nr-reporting-summary-flat.pdf

Life sciences study design

All studies must disclose on these points even when the disclosure is negative.

Sample size	No prior sample size determination was conducted. All experiments were conducted in at least 2 biological replicates. Statistical testing ensured significant findings.
Data exclusions	No replicates were excluded, and all attempts to replicate were successful.
Replication	All experiments were conducted in at least 2 biological replicates. For all sequencing data-types, successful replication has been confirmed with Principal Component Analysis.
Randomization	Randomization was relevant to the study, because the difference between healthy and disease was assessed.
Blinding	The investigators were not blinded to sample group allocation, because the difference between healthy and disease was assessed. Sample group assignments were further ensured using Principal Component Analysis on all relevant sequencing data.

Reporting for specific materials, systems and methods

We require information from authors about some types of materials, experimental systems and methods used in many studies. Here, indicate whether each material, system or method listed is relevant to your study. If you are not sure if a list item applies to your research, read the appropriate section before selecting a response.

Materials & experimental systems	Methods
n/a <input type="checkbox"/> Involved in the study <input checked="" type="checkbox"/> Antibodies <input type="checkbox"/> Eukaryotic cell lines <input checked="" type="checkbox"/> Palaeontology <input type="checkbox"/> Animals and other organisms <input checked="" type="checkbox"/> Human research participants <input checked="" type="checkbox"/> Clinical data	n/a <input type="checkbox"/> Involved in the study <input checked="" type="checkbox"/> ChIP-seq <input checked="" type="checkbox"/> Flow cytometry <input checked="" type="checkbox"/> MRI-based neuroimaging

Antibodies

Antibodies used	CTCF (D31H2; Cell Signaling Catalog no: 3418; lot 3 &4); H3K27ac (Active motif; Catalog no: 39133, Lot no: 01518010); c-MYC (D84C12; Cell Signaling; Catalog no: 5605, dilution 1:500) Lot no: 15; Actin (Millipore, clone C4, Catalog no: MAB1501R, Lot no: 2819194, dilution 1:3000)
Validation	Validation of antibodies is ensured by commercial manufacture for the application used. For CTCF antibody from Cell Signaling, the datasheet for validation is available at https://media.cellsignal.com/pdf/3418.pdf For H3K27ac antibody from Active motif, the datasheet for validation is available at https://www.activemotif.com/documents/tds/39133.pdf For, C-MYC, the validation is available in https://media.cellsignal.com/pdf/14819.pdf

Eukaryotic cell lines

Policy information about [cell lines](#)

Cell line source(s)	The CUTLL1 and Jurkat cell lines were a gift from Adolfo Ferrando's lab at Columbia.
Authentication	Cell lines have been authenticated by PCR detection of originally described translocations, detection of intra-nuclear NOTCH1 and sensitivity to originally described drugs
Mycoplasma contamination	Cell lines were tested negative for mycoplasma.

Commonly misidentified lines
(See [ICLAC](#) register)

The cell lines used in this study are not listed on the ICLAC list of commonly misidentified cell lines.

Animals and other organisms

Policy information about [studies involving animals](#); [ARRIVE guidelines](#) recommended for reporting animal research

Laboratory animals	NOD-SCID-IL2rg ^{-/-} (NSG) mice between 4 to 8 weeks age
Wild animals	This study did not include wild animals.
Field-collected samples	This study did not include field-collected samples.
Ethics oversight	All animal experiments were performed in accordance with protocols approved by the New York University Institutional Animal Care and Use Committee.

Note that full information on the approval of the study protocol must also be provided in the manuscript.

Human research participants

Policy information about [studies involving human research participants](#)

Population characteristics	Additional co-variates (age, gender, diagnosis, mutational status) are listed in Supplementary Information.
Recruitment	Healthy T cells have been ordered commercially. Leukemia samples have been selected for two specific sub-types but potential biases are discussed in Figure 1 and Supplementary Information combining mutation status, expression and chromatin interaction information.
Ethics oversight	Samples were collected by Columbia Presbyterian Hospital or Weill Cornell Medical College with informed consent and approved and analyzed under the supervision of the Columbia University Medical Center Institutional Review Board or Weill Cornell Medical College Institutional Review Board.

Note that full information on the approval of the study protocol must also be provided in the manuscript.

ChIP-seq

Data deposition

Confirm that both raw and final processed data have been deposited in a public database such as [GEO](#).

Confirm that you have deposited or provided access to graph files (e.g. BED files) for the called peaks.

Data access links

May remain private before publication.

ChIP-Seq data was deposited at NCBI GEO under accession GSE115893. Token: ujmpiasozxstlw
https://urldefense.proofpoint.com/v2/url?u=https%3A__www.ncbi.nlm.nih.gov_geo_query_acc.cgi-3Facc-3DGSE115893&d=DwIBAg&c=j5oPpO0eBH1io48DtedbOBGmuw5jHLjgvtN2r4ehE&r=N0slyiNu-4hMYPy11ZY72eU4uF0KhiHRWO11zlklvq8&m=ly2Owf8yNQMY1mdVP20avxkH3kmKtebTIULDAOM4kl&s=rAFpbkjssrbSbe1AcbHad26xqxTtHhbyUuhv5relf8&e=

Files in database submission

T cell CTCF rep1
 T cell CTCF rep2
 T-ALL1 CTCF rep1
 T-ALL1 CTCF rep2
 T-ALL2 CTCF rep1
 T-ALL2 input
 Jurkat CTCF rep1
 Jurkat CTCF rep2
 Jurkat input
 CUTLL1 CTCF rep1
 CUTLL1 CTCF rep2
 CUTLL1 CTCF rep3
 CUTLL1 CTCF rep4
 CUTLL1 CTCF rep5
 CUTLL1 H3K27ac rep1
 CUTLL1 H3K27ac rep2
 CUTLL1 H3K27ac rep3
 CUTLL1 H3K27ac rep4
 CUTLL1 gSI H3K27ac rep1
 CUTLL1 gSI H3K27ac rep2
 CUTLL1 THZ1 H3K27ac rep1
 CUTLL1 THZ1 H3K27ac rep2

Methodology

Replicates

CTCF:
 T cells 2 replicates + 1 input
 T-ALL 1 as 2 replicates + 1 input
 T-ALL 2 as 1 replicates + 1 input
 CUTLL1 DMSO as 5 replicates + 1 input
 CUTLL1 gSI as 3 replicates + 1 input
 Jurkat as 2 replicates + 1 input

H3K27ac:
 CUTLL1 DMSO as 2 replicates + 1 input
 CUTLL1 gSI as 2 replicates + 1 input
 CUTLL1 THZ1 as 2 replicates + 1 input

Sequencing depth

Sequencing depth is detailed in Supplementary Table 1.

Antibodies

CTCF (D31H2; Catalog no: 3418, lot 3 and 4); Lot no:; 10 ug antibody used per IP
 H3K27ac (Active motif; Catalog no: 39133) ; Lot no: Lot no: 01518010, 5ug antibody used per IP

Peak calling parameters

MACS2 parameters for CTCF: --nomodel --extsize=200 --qvalue 0.05
 MACS2 parameters for H3K27ac: --broad --nomodel --extsize=200 --qvalue 0.05 --broad-cutoff 0.05

using -c option to specify input samples

Data quality

Based on merged peaks and peak strength, we performed Principal Component Analysis to ensure replication.

Total number of peaks detected with above peak-calling approach:

T cells CTCF: 34443
 T-ALL 1 CTCF: 28730
 T-ALL 2 CTCF: 64059
 CUTLL1 CTCF: 25213
 CUTLL1 gSI CTCF: 18111
 Jurkat CTCF: 15196
 CUTLL1 H3K27ac: 30726
 CUTLL1 gSI H3K27ac: 25309
 CUTLL1 THZ1 H3K27ac: 30542

Software

Read alignment: Reads were aligned against the reference sequence hg19 with bowtie2 (version 2.3.1) with standard parameters and only uniquely mapped reads were kept with MAPQ > 20.

Deduplication: Aligned reads were filtered for duplicated reads using picard-tools version 2.6.0.

Peak-calling: Peak calling for CTCF and H3K27ac was performed using MACS2 (version 2.0.1) using narrow (CTCF) and broad (--broad; H3K27ac) option (sepcial parameters: --no-model).

Differential binding: To identify differentially bound peaks, we performed diffBind (version 2.2.12) analysis, using the normalization option DBA_EDGER.

Bigwig: For visualization purposes, we generated fold-enrichment bigwig files by applying MACS2 (version 2.0.1) bdgcmp over input (-m FE)